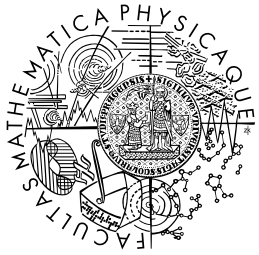

FACULTY
OF MATHEMATICS
AND PHYSICS
Charles University

MASTER THESIS

Antonín Bad'ura

Magnetooptical and magnetotransport effects in non-collinear antiferromagnets

Department of Chemical Physics and Optics

Supervisor of the master thesis: RNDr. Eva Schmoranzerová, Ph.D.
Study programme: Physics
Study branch: Optics and Optoelectronics

Prague 2022

I declare that I carried out this master thesis independently, and only with the cited sources, literature and other professional sources. It has not been used to obtain another or the same degree.

I understand that my work relates to the rights and obligations under the Act No. 121/2000 Sb., the Copyright Act, as amended, in particular the fact that the Charles University has the right to conclude a license agreement on the use of this work as a school work pursuant to Section 60 subsection 1 of the Copyright Act.

In ..... date ....

Author's signature

Acknowledgements

This thesis could not be completed without the substantial help of others. First of all, I would like to thank Eva Schmoranzerová for her careful and supportive guidance and everyday help.

I also want to express my gratitude to the whole group of Sebastian T. B. Goennenwein at the University of Konstanz, as they created an enjoyable and supportive environment during my research stay. Namely, I would like to thank Melek Villanueva, Michi Lammel, and Marvin Weiss for their support, sharing of ideas, and everyday fun. My special thanks go to Sebastian Goennenwein himself for enabling me to stay in his group and for his guidance during my four months in Germany.

The magnetooptical experiments could not have been finished without the help of Martin Veis from the Institute of physics from the Faculty of mathematics and physics, who enabled me to use his labs and gave us supportive feedback on the results of our experiments.

I am also grateful to our foreign collaborators for their support, namely to Lisa Michez from the Centre Interdisciplinaire de Nanoscience from Marseille for growing the samples and to Rafael Lopes Seeger from the Spintec in Grenoble for the lithographic fabrication of the devices.

Special thanks belong to Helena Reichlová, who was anytime everywhere for her tireless support.

Title Magnetooptical and magnetotransport effects in non-collinear antiferromagnets

Author Antonín Bad'ura

Department Department of Chemical Physics and Optics

Supervisor RNDr. Eva Schmoranzerová, Ph.D., Department of Chemical Physics and Optics

Abstract In this thesis, we investigate the magnetic properties of an antiferromagnet Mn_5Si_3. Mn_5Si_3 shows two configurations of magnetic moments depending on temperature: the low-temperature phase (below 90 K) is noncollinear and noncoplanar, while the spin configuration is collinear at higher temperatures up to 240 K. Furthermore, the band structure of Mn_5Si_3 is spin-split in both antiferromagnetic phases via a specific nonrelativistic mechanism, referred as altermagnetism. We probed this spin-splitting by two distinct methods: Firstly, we characterized the transport properties of Mn_5Si_3 by measuring electronic and thermoelectric transport phenomena. Particularly, we detected the spontaneous Hall and Nernst responses in Mn_5Si_3 thin epitaxial films. The key outcome was a detailed analysis of the spontaneous Hall signal together with the observation of the spontaneous Nernst effect. In the second approach, we studied magnetooptical response of the thin films, where we focused on reflective geometry (the polar Kerr effect and the Voigt effect). We observed a pronounced signal in the Voigt geometry, which is quadratic in magnetization and could correspond to a magnetooptical signal. Furthermore, we observed a change in optical response when the thin-film samples were exposed to a thermally-induced mechanical strain. The results indicate that Mn_5Si_3 shows an altermagnetic phase which can be analyzed using electronic and thermoelectric transport. Magnetooptical methods revealed some potential, however, further experiments are needed to confirm the origin of the observed optical signals.

Keywords altermagnetism, Hall effect, Nernst effect, magnetooptical Kerr effect, Voigt effect.

Contents

Introduction

Conventional semiconductor electronics and its rapid development since its origin in the 1950s induced enormous technological progress that influenced every aspect of human life. This rapid evolution was underpinned by the concept of Moore's law, a techno-economic model that has enabled the manufacturers to double the performance of the electronic components every two years within a fixed cost, power, and chip size [1]. However, as miniaturization approaches the atomic scale, the technological process faces its physical limits, and no further improvement is projected anymore [1]. There are multiple ways of addressing this issue that could preserve the performance scaling with no need for further lithographic minituarization. These new paths include new materials and more efficient device designs, or even completely novel models of computational architectures, such as neuromorphic computing [2]. One of the promising directions turned out to be *spintronics*, a spin-based electronics that employs the spin-degree of freedom of the electron in the data storage and processing [3]. The advantages promised by spintronic devices include nonvolatility of the data storage, increased data processing speed, and decreased electric power consumption [3].

Multiple technological achievements were already obtained since the proposal of the concept of spintronics in the 1980s. These include the hard disk drive read heads based on giant magnetoresistance or the magnetoresistive random access memory using the magnetic tunnel junction effect and the effect of spin-transfer torque [4].

Spintronic devices have been traditionally based on ferromagnetic materials. However, recently a new field of spintronics has emerged where antiferromagnets replace the conventional ferromagnetic layers. The antiferromagnetic materials provide numerous advantages for spin electronics because of the interesting features they combine: They are robust against perturbations by an external magnetic field while being free of a stray field effect; they are expected to show ultrafast dynamics of magnetic moments, and importantly, can generate magnetotransport effects of similar strength as the conventional ferromagnets [5]. The proof-of-principle antiferromagnetic memory was demonstrated in 2016 [6].

This thesis aims to contribute to antiferromagnetic spintronics research by focusing on a specific class of materials with antiferromagnetic ordering that shows nonrelativistic spin splitting. These materials have been introduced only very recently, and the term *altermagnetism* was established to describe them [7]. An example of such material is an intermetallic antiferromagnet Mn_5Si_3 that we study in our work by two distinct approaches. Namely, we use the methods of magnetooptics and magnetotransport to characterize the response of Mn_5Si_3

epilayers to the applied external magnetic field and to study the nature of the novel magnetic ordering in this system.

The thesis is divided into three main chapters. The first chapter serves as a theoretical introduction to the concept of magnetic order in solids. We cover the origins of magnetic ordering, types of magnetically ordered materials, and we also introduce the concept of altermagnetism. Finally, we also present the antiferromagnetic compound Mn_5Si_3. The following two chapters are dedicated to the two experimental methods we used to study the magnetic properties of Mn_5Si_3: the measurement of magnetotransport properties and a magnetooptical study. In each of these chapters, we explain the theoretical basis of the experiments, describe the experimental methods, and discuss the results.

Chapter 1

Antiferromagnetism and Mn_5Si_3

In this introductory chapter, we provide a description of theoretical concepts related to magnetic order and its origin. We also review altermagnetism, a novel type of magnetic ordering, together with a particular member of this class, Mn_5Si_3.

1.1 Origins of magnetic order

The elementary quantity of the solid state magnetism is a dipole magnetic moment $\boldsymbol{m}$. In classical electromagnetism, we can represent it by an infinitesimally small current loop. A generalized relationship between the magnetic moment and the current density $\boldsymbol{j}$ is classically formulated as follows ($\boldsymbol{r}$ is radius vector):

$$\boldsymbol{m} = \frac{1}{2} \int \boldsymbol{r} \times \boldsymbol{j}(\boldsymbol{r}) \, \mathrm{d}^3 r, \tag{1.1}$$

In solids, it is useful to introduce magnetization $\boldsymbol{M}$ as a local average of the magnetic moment in a mesoscopic volume δV:

$$\delta \boldsymbol{m} = \boldsymbol{M}(\boldsymbol{r}) \, \delta V. \tag{1.2}$$

Magnetization can represent a spontaneous moment of a ferromagnetic domain or the uniform magnetization of a paramagnet induced by the applied magnetic field.

Magnetic moment and magnetization are both axial vectors (tensors, strictly speaking) which means that they change sign under the time-reversal $t \to -t$ but stay unchanged under the spatial inversion $\boldsymbol{r} \to -\boldsymbol{r}$. This is a completely distinct behaviour from the standard polar vectors, such as position or current density, that experience a sign change also for the spatial inversion.

The magnetic field $\boldsymbol{B}$ is related to magnetization and the field intensity $\boldsymbol{H}$ through the standard formula:

$$\boldsymbol{B} = \mu_0 \, (\boldsymbol{H} + \boldsymbol{M}) = \mu_0 \, (1 + \hat{\chi}) \, \boldsymbol{H} = \hat{\mu} \, \boldsymbol{H}, \tag{1.3}$$

where we introduced material-dependent permeability $\hat{\mu}$ and magnetic susceptibility $\hat{\chi}$. Generally speaking, both of these variables are tensors, and $\hat{\chi}$ plays particularly an important role when describing magnetically ordered materials, as shall be explained in the following section.

The origin of magnetic moments in solids is associated with electrons and their angular momentum. An electron gains orbital momentum from two distinct sources: orbital motion and spin [8]. To describe the mutual interaction of these momenta and their interaction with the magnetic field, one needs to employ quantum mechanics and particularly, the Schrödinger equation.

The time-dependent Schrödinger equation $\mathcal{H}\psi = i\hbar\dot{\psi}$ is not relativistically invariant. This issue was solved by Dirac, who introduced the relativistic quantum-mechanical theory of fermions described by the Dirac equation [9]. Dirac also showed that the spin of an electron naturally emerges when incorporating special relativity into quantum mechanics [9].

Assuming the presence of an electromagnetic field, the nonrelativistic limit of the Dirac equation can be represented by the Hamiltonian for a single electron [8]:

$$\mathcal{H} = \left(\frac{1}{2m}\left(\hat{\boldsymbol{p}} + e\boldsymbol{A}\right)^2 - e\phi(\boldsymbol{r})\right) - \frac{p^4}{8m_e^3c^2} + \frac{e}{m_e}\left(\nabla \times \boldsymbol{A}\right)\cdot\hat{\boldsymbol{s}} - \\ - \frac{e}{2m_e^2c^2r}\frac{\mathrm{d}\phi}{\mathrm{d}r}\hat{\boldsymbol{l}}\cdot\hat{\boldsymbol{s}} + \frac{e}{4m_e^2c^2}\frac{\mathrm{d}\phi}{\mathrm{d}r}, \quad (1.4)$$

where $\boldsymbol{A}$ and ϕ are the vector and scalar potentials, $\hat{\boldsymbol{p}}$ is the momentum operator, $\hat{\boldsymbol{s}} = \hbar/2\,\hat{\boldsymbol{\sigma}}$ is the spin operator for $\hat{\boldsymbol{\sigma}}$ being the vector of Pauli matrices, and $\hat{\boldsymbol{l}} = \hat{\boldsymbol{r}} \times \hat{\boldsymbol{p}}$ is the angular momentum operator.

The first term in Eq. (1.4) corresponds to the nonrelativistic Hamiltonian of an electron in an electromagnetic field, described by potentials ϕ and $\boldsymbol{A}$, the second term represents a high-order relativistic correction to the kinetic energy. The third term is the interaction of the electron spin with the electromagnetic field. When combining the terms, including interaction of spin with the external electromagnetic field (i.e., the first and the third terms), this gives the complete expression for the *Zeeman interaction* with a Hamiltonian $\mathcal{H}_z$:

$$\mathcal{H}_Z = \frac{e}{2m_e}\left(\hat{\boldsymbol{l}} + g_s\hat{\boldsymbol{s}}\right)\cdot\boldsymbol{B}, \quad (1.5)$$

where $g_s \approx 2.00$ is the anomalous gyromagnetic ratio of a free electron. The fourth term of Eq. 1.4 describes the *spin-orbit interaction* which for a central potential can be written as:

$$\mathcal{H}_{SO} = \lambda\,\hat{\boldsymbol{l}}\cdot\hat{\boldsymbol{s}}, \quad (1.6)$$

where $\lambda = -Ze^2\mu_0/(8\pi m_e^2 r^3)$ (Ze is the nuclear charge). The last term is a correction term [8].

Apparently, the relativistic theory of an electron gives rise to new, spin-related interactions. In terms of the microscopic theory of magnetism, the prominent term is the spin–orbit interaction (SOI) which is the origin of interesting phenomena, including magnetocrystalline anisotropy, anisotropic magnetoresistance, and the spin Hall effect [8]. However, to describe such effects, we need to move from a single-electron problem to the model of many electrons localized on an atom.

When considering an isolated many-electron ion, the nonrelativistic Hamiltonian of an electron $\mathcal{H}_0$ has to include the Coulomb interaction with the nucleus and the other electrons [8]:

$$\mathcal{H}_0 = \sum_i\left[\frac{1}{2m_e}\left(\hat{\boldsymbol{p}} + e\boldsymbol{A}\right)^2 - e\phi(\boldsymbol{r}_i) - \frac{Ze^2}{4\pi\varepsilon_0 r_i}\right] + \sum_{i<j}\frac{e^2}{4\pi\varepsilon_0 r_{ij}}, \quad (1.7)$$

where i, j numbers the individual electrons. The eigenfunctions of this Hamiltonian correspond in the absence of an external magnetic field to the electronic orbitals of an atom. The electronic states in the orbitals are characterized by a unique set of quantum numbers, which also includes the spin number s_i and the angular momentum number l_i. These momenta are coupled, giving the total orbital quantum numbers $S = \sum_i s_i$ and $L = \sum_i l_i$ [8].

The filling of the orbitals with electrons in the ground state follows a phenomenological prescription formulated by Hund in the form of three Hund's rules. The first rule minimizes the Coulomb interaction among electrons which is achieved by maximizing the total spin number S. The second rule requires maximizing L, consistently with S. The final rule expresses the total angular momentum J depending on the filling of a shell: if the shell is less than half full, $J = L - S$. If it is exactly half full $J = 0$ and more than a half-full shell results in $J = L + S$ [8].

The magnetic moment of an isolated ion is related to the total angular momentum $\boldsymbol{J}$ as:

$$\boldsymbol{m} = -\frac{e}{2m_e}\, g\boldsymbol{J}, \tag{1.8}$$

where g is the Landé factor [8]. Therefore, ions with $J = 0$ do not have their own magnetic moment and are nonmagnetic.

So far, we have been considering either a single electron or an isolated ion. However, in the context of this work, a crystalline solid is a more relevant system to describe. There is a significant difference as compared to the isolated ions, as the interaction between the electronic charge distribution of an atom $\rho_0(\boldsymbol{r})$ and the surrounding charges in the crystal lattice emerges. Potential of the surrounding charges is usually described by the crystal-field potential $\varphi_{ef}(\boldsymbol{r})$, and the resulting crystal-field interaction with ρ_0 can be expressed by the Hamiltonian $\mathcal{H}_{ef}$ [8]:

$$\mathcal{H}_{ef} = \int \rho_0(\boldsymbol{r})\, \varphi_{ef}(\boldsymbol{r})\, \mathrm{d}^3 r. \tag{1.9}$$

The complete Hamiltonian of an electron in a crystalline solid has then four terms:

$$\mathcal{H} = \mathcal{H}_0 + \mathcal{H}_{SO} + \mathcal{H}_Z + \mathcal{H}_{ef}, \tag{1.10}$$

with $\mathcal{H}_{SO}$ and $\mathcal{H}_Z$ being the known spin-orbit and Zeeman terms, respectively. $\mathcal{H}_0$ is the above-defined Hamiltonian of an electron in an isolated ion.

As we have shown, atoms can have their own magnetic moment depending on their electronic structure. Magnetic ordering of these moments depends on their mutual interaction. Multiple mechanisms can mediate the magnetic interaction, but the most straightforward mechanism is the exchange interaction.

Consider a simple model of two electrons. Their mutual wave function can form either a singlet state $S = 0$ with the corresponding energy E_S or a triplet state $S = 1$ with E_T. The mutual interaction of their spins represented by the operators $\hat{\boldsymbol{s}}_1$ and $\hat{\boldsymbol{s}}_2$ can be described by the Hamiltonian:

$$\mathcal{H}_S = -2J\, \hat{\boldsymbol{s}}_1 \cdot \hat{\boldsymbol{s}}_2, \tag{1.11}$$

where $J = (E_S - E_T)/2$ is called the exchange integral [10]. If J is positive, the triplet state is preferred and the spins are aligned parallel. When $J < 0$, the

singlet state dominates and the spins align antiparallel. For a many-electron problem, Eq. (1.11) can be rewritten as:

$$\mathcal{H}_S = -\sum_{i,j} J_{ij}\, \hat{\boldsymbol{s}}_i \cdot \hat{\boldsymbol{s}}_j. \tag{1.12}$$

The calculation of the exchange integral is rather complicated, but some general features were observed [10]: For electrons located at the same atom, J_{ij} is usually positive, resulting in the preference for a parallel alignment of the spins (this is consistent with the first Hund's rule). Because of the Pauli exclusion principle, the electrons are localized, and their wave functions do not overlap. In contrast, the exchange integral tends to be negative for the electrons localized on neighbouring atoms, and the antiparallel configuration is preferred.

If the electron on the neighbouring magnetic atoms interacts via the exchange interaction, the mechanism of magnetic interaction is called a *direct exchange*. However, this interaction is often weak due to the insufficient direct overlap of the neighbouring magnetic orbitals [10]. In such a situation, indirect exchange interactions often take place.

Due to an indirect exchange, the interaction between the magnetic atoms may occur even if they are not directly neighbouring. This is enabled by the *superexchange* where a nonmagnetic ion mediates the exchange interaction. The superexchange usually results in an antiferromagnetic ordering of the spins that allows the electrons to become delocalized over the crystal, thus lowering the kinetic energy [10].

In some oxides, ferromagnetic exchange interaction can arise due to the mixed valency of the magnetic ion (e.g., manganese that can exist both as Mn^{3+} and Mn^{4+}). This mechanism is called a *double exchange* as the atoms with different valencies share a valence electron, which lowers the kinetic energy. However, this sharing is possible only in the situation where the neighbouring atoms are ferromagnetically aligned [10].

The last type of the exchange mechanisms, *Dzyaloshinsky–Moriya interaction*, originates in the exchange interaction between the ground state of a magnetic atom and the excited state of its neighbour, where the excitation is caused by the spin–orbit interaction. When acting between two spins $\hat{\boldsymbol{s}}_1$ and $\hat{\boldsymbol{s}}_2$, it leads to the Hamiltonian $\mathcal{H}_{DM}$ [10]:

$$\mathcal{H}_{DM} = \boldsymbol{D} \cdot (\hat{\boldsymbol{s}}_1 \times \hat{\boldsymbol{s}}_2)\,, \tag{1.13}$$

where the vector $\boldsymbol{D}$ vanishes in the systems with the space inversion symmetry. The interaction forces $\hat{\boldsymbol{s}}_1$ and $\hat{\boldsymbol{s}}_2$ to be perpendicuar to each other. It commonly occurs in antiferromagnets where it cants the antiferromagnetically ordered spins in such a way that a small ferromagnetic moment arises. Such materials are known as *weak ferromagnets*.

Now it is evident that atoms may have their own magnetic moment originating in their electronic structure. In a crystalline solid, these moments interact through a multitude of exchange mechanisms, resulting in moments being aligned parallel or antiparallel. The resulting magnetic order is the topic of the following section.

1.2 Magnetic structure in solids

The previous section showed that a non-zero magnetic moment was a necessary condition for atoms in a crystalline solid to mediate magnetic interaction. Zero magnetic moment results in the material being *diamagnetic*, i. e. having negative magnetic susceptibility. If the material contains local permanent magnetic moments, but the coupling among them is weak, we speak about *paramagnetism*. The magnetic structure is disordered in paramagnetic materials due to the thermal fluctuations; however, the moments align when an external magnetic field is applied, resulting in non-zero magnetization along the applied field. If the magnetic interaction between ions is strong enough to overcome the thermal fluctuations, the moments can align spontaneously. When this spontaneous alignment results in moments in a parallel configuration, the ordering is *ferromagnetic* resulting in finite magnetization. In *antiferromagnets*, the magnetic structure consists of two or more sublattices with parallel ordering that are mutually antiparallel, which sum together to zero net magnetization. There are also *ferrimagnets* with multiple sublattices that do not fully compensate each other, which results in finite magnetization, generally much weaker than in the case of the ferromagnets. The susceptibility of materials with permanent magnetic moments (i. e. also including paramagnets) is positive. Let us now have a closer look at each of these individual types of magnetic ordering.

Diamagnetism Orbital diamagnetism is an effect that is present to some extent in every atom and molecule [8]. A semiclassical expression for the diamagnetic susceptibility of electrons with an orbital moment can be deduced from the Larmor precession. When such electron is placed in an external magnetic field, precession of the electron is induced, resulting in a magnetic moment that opposes the applied field (a direct consequence of the well-known Lenz's law). This generates a negative contribution to susceptibility. Although orbital diamagnetism is a small effect, it dominates in materials with fully filled electronic shells [8].

Paramagnetism Unpaired electrons in an atom's shells result in a non-zero magnetic moment, as discussed earlier. In a paramagnet, these moments are randomly oriented in the absence of a magnetic field. The magnetic field lines them up, resulting in finite net magnetization that depends on the field strength.

Temperature dependence of paramagnetic susceptibility can be easily derived for localized electrons when we suppose their Boltzmann distribution. If $n^{\uparrow}$ is the concentration of electrons with the moment along the applied field and $n^{\downarrow}$ are electrons with the opposite moment, the induced magnetization M is [8]:

$$M = (n^{\uparrow} - n^{\downarrow})\,\mu_B = \alpha\left(e^{\frac{\mu_B B}{k_B T}} - e^{\frac{-\mu_B B}{k_B T}}\right) = n\mu_B \tanh\frac{\mu_B B}{k_B T}, \tag{1.14}$$

where $\alpha e^{\frac{\mu B}{k_B T}}$ is the Boltzmann distribution of electrons with the moment μ, α is a proportionality constant, and $n = (n^{\uparrow} + n^{\downarrow})$. At high temperatures, we can replace the *tanh* function in Eq. (1.14) by its argument which results in the following temperature dependence of susceptibility, called the Curie law [8]:

$$\chi = \frac{\mu_0 M}{B} = \frac{n\mu_0\mu_B^2}{k_B T} = \frac{C}{T} \tag{1.15}$$

with the Curie constant C. Apparently, the susceptibility diverges for $T \to 0$ as illustrated in Fig. 1.1.

Note that another contribution to susceptibility exists, related to the delocalized electrons described by Pauli. The Pauli susceptibility is temperature-independent to the first order and is about two orders of magnitude smaller than the Currie susceptibility at room temperature [8].

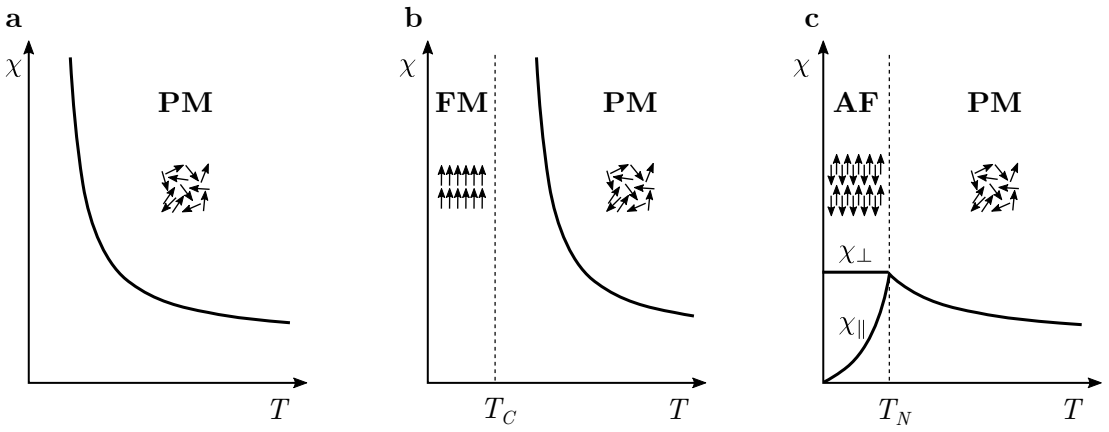

Figure 1.1: Temperature dependence of susceptibility for **a** a paramagnet (PM), **b** a ferromagnet (FM) with the Curie temperature T_C, and **c** an antiferromagnet (AF) with the Néel temperature T_N. Adapted from [11].

Ferromagnetism The characteristic feature of ferromagnets is their spontaneous magnetization which is a result of the mutual interaction among the individual magnetic moments. The interaction is strong enough to overrule thermal fluctuations, which holds up to the Curie temperature when the ordering collapses and the material becomes paramagnetic. The magnetization of a ferromagnet tends to lie along the easy direction, determined by the crystal structure and the sample shape.

The spontaneous alignment of the moments was first explained by Weiss, who introduced an internal "molecular field" that is proportional to the magnetization [8]. Later, it was revealed that this internal field, which was in the order of magnitude of hundreds of tesla, actually does not exist [11]. Despite that, Weiss' molecular field is a useful instrument which allows for predicting the Curie temperature of the given ferromagnet.

As the molecular field is proportional to magnetization, the internal molecular field $\boldsymbol{H}^i$ can be expressed as:

$$\boldsymbol{H}^i = n_W \boldsymbol{M} + \boldsymbol{H}, \tag{1.16}$$

where n_W is a proportionality constant and $\boldsymbol{H}$ is the external magnetic field. Magnetization in Eq. (1.16) is determined by the Brillouin function (see e.g. Ref. [8]) which leads to the Curie temperature T_C expressed as [8]:

$$T_C = n_W \frac{\mu_0 n g^2 \mu_B^2}{3k_B} J(J+1), \tag{1.17}$$

where J is the total angular momentum, g is the Landé g-factor, and n is the concentration of electrons. The paramagnetic susceptibility above T_C is given by the Curie–Weiss law:

$$\chi = \frac{C}{T - \theta_p}, \tag{1.18}$$

where $\theta_p = T_C$ is the Curie temperature within the molecular field theory [8]. The Curie–Weiss law is illustrated in Fig. 1.1b.

For temperatures below T_C, magnetization of a ferromagnet is non-zero, and it becomes identically zero at T_C when no external field is applied. The magnetization is a continuous function of temperature at T_C, which classifies the transition between the ferromagnetic and paramagnetic phase as the second-order phase transition [10].

As already mentioned, the molecular-field theory, though a useful qualitative tool, is not correct in its assumptions. The true origin of the effective field $\boldsymbol{H}^i$ is the exchange interaction along with the Pauli principle as described in the previous section.

Antiferromagnetism If the exchange interaction is negative, i.e. the exchange integral $J_{ij} < 0$ in Eq. (1.12), the magnetic moments tends to align antiparallel. Negative exchange interaction results in a magnetic ordering with two sublattices with oppositely oriented spins. Net magnetization of the material is zero. This behaviour describes the *collinear antiferromagnetism*. The magnetic order persists at temperatures $T < T_N$ and disappears at the Néel temperature T_N, where the material usually becomes paramagnetic. However, materials with a direct transition from an antiferromagnetic to a ferromagnetic state (such as FeRh), though rare, also exist [12]. The collinear, parallel antiferromagnetism is not the only possibility of magnetic order with zero magnetization. There are also *noncollinear antiferromagnets* where the magnetic spins are not parallel to each other but have a more complicated configuration.

Similarly to the ferromagnets, the molecular field model can be used to describe magnetic behaviour of the collinear antiferromagnets. We suppose that the magnetic structure contains two sublattices A and B with the corresponding magnetizations $\boldsymbol{M}_A = -\boldsymbol{M}_B$. In order to describe the interaction between the sublattices, we introduce a negative Weiss coefficient $n_{AB} = n_{BA}$ for the interlattice interaction, together with $n_{AA} = n_{BB}$ that describes the intralattice interaction [8].

The internal effective magnetic fields $\boldsymbol{H}_A^i$ and $\boldsymbol{H}_B^i$ can be then expressed as:

$$\boldsymbol{H}_A^i = n_{AA}\,\boldsymbol{M}_A + n_{AB}\,\boldsymbol{M}_B + \boldsymbol{H}, \tag{1.19}$$

$$\boldsymbol{H}_B^i = n_{BA}\,\boldsymbol{M}_A + n_{BB}\,\boldsymbol{M}_B + \boldsymbol{H}, \tag{1.20}$$

where $\boldsymbol{H}$ is the contribution from an external magnetic field [8]. Using the Curie law for a paramagnet in Eq. (1.15), the Néel temperature T_N and the paramagnetic temperature θ_p can be expressed using the Curie coefficient C [8]:

$$T_N = \frac{C}{2}\left(n_{AA} - n_{AB}\right), \tag{1.21}$$

$$\theta_p = \frac{C}{2}\left(n_{AA} + n_{AB}\right). \tag{1.22}$$

Since $n_{AB} < 0$, the paramagnetic temperature is smaller than T_N and is usually negative. The Curie–Weiss law in Eq. (1.18), on the other hand, remains valid. Supposing that there are no intralattice interactions, i. e. $n_{AA} = n_{BB} = 0$, it can be rewritten as [8]:

$$\chi = \frac{C}{T + T_N}. \tag{1.23}$$

If a small magnetic field is applied to a collinear antiferromagnet that is parallel to the magnetization of the sublattices, the corresponding susceptibility $\chi_\parallel$ can be calculated by expanding the Brillouin function around zero field (for details, see Ref. [8]). The temperature dependence of $\chi_\parallel$ is an increasing function until T_N is reached, as illustrated in Fig. 1.1c. If the field is applied perpendicularly to the magnetization direction, the corresponding susceptibility is temperature-independent, as also shown in Fig. 1.1c [8].

So far, we have described the collinear antiferromagnets where the moments are ordered parallel to each other. However, some antiferromagnets have a more complicated spin structure, although still satisfying that net magnetization is zero —*noncollinear antiferromagnets*. This ordering stems from the fact that in certain systems, the antiferromagnetic interactions cannot always be satisfied (unlike the ferromagnetic interactions) [8]. A good example represents a triangular crystal lattice with antiferromagnetically-coupled moments in the vertices, as demonstrated in Fig. 1.2. If the moments had to be ordered antiferromagnetically in a collinear way and, for example, moment α points down and β up, the moment γ would be frustrated since it is antiferromagnetically coupled to both the moments and there would be no preferred position (see Fig. 1.2a). In such a situation, there are two possible solutions for the lowest energy of the system, in which the moments have a noncollinear arrangement, as shown in Figs. 1.2b,c [13]. Notice that although the moments are not mutually parallel, net magnetization of the system is still zero. Similar frustration can also arise for other crystalline lattices such as the kagome, cubic face-centred, or tetrahedral lattice [8].

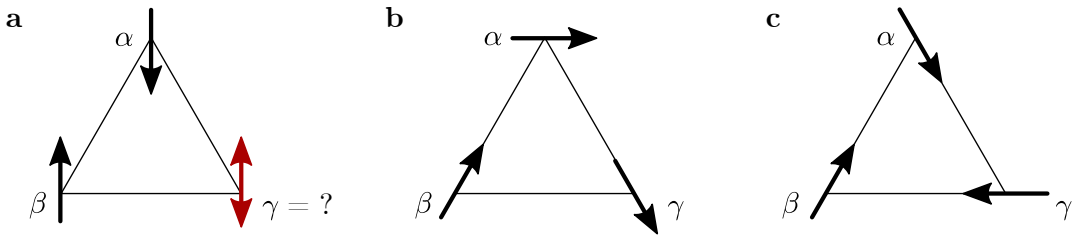

Figure 1.2: Frustrated antiferromagnetic moments within a triangular lattice. **a** Collinear configuration causes frustration of the moment γ because of the competing exchange with α and β. **b** and **c** Two possible configurations without frustration with lowest energy resulting in noncollinear ordering. Adapted from [13].

In noncollinear antiferromagnets, the frustration is usually removed by the magnetocrystalline anisotropy or by the Dzyaloshinsky–Moriya interaction, resulting in a stable noncollinear magnetic order [14–17]. Furthermore, the frustration may lead to an even more complex spin configuration where the magnetic moments are not ordered in one plane. Such magnetic structure would then be called noncoplanar and represents one of the most complex systems from the theoretical point of view.

1.3 Altermagnetism

In the previous section, we discussed various types of magnetic order based on the mutual arrangement of local magnetic moments. This approach covers conventional collinear spin structures like ferromagnets or antiferromagnets, as well as the more complex noncollinear systems such as magnetic skyrmions. In the past years, a complementary strategy of describing magnetic structure in solids based on their electronic band structure appeared [18]. This change of approach from the real to the reciprocal space was motivated by new phenomena related to the topological aspects of the electronic states [19] or by the momentum-dependent spin splitting of electronic bands in collinear antiferromagnets [18, 20]. The latter phenomenon has recently gained considerable attention since it was predicted in materials based on the light elements [21, 22] where the most common source of the band splitting, the spin–orbit interaction, is usually weak [18]. To distinguish such collinear antiferromagnets with nonrelativistic spin-splitting from conventional collinear antiferromagnets, Šmejkal et al. introduced a new name *altermagnetism* [7].

Up to now, the formalism of magnetic-symmetry groups has guided the search for novel magnetic materials and has been broadly applied in the research of equilibrium and non-equilibrium phenomena related to the magnetic order [7]. However, these groups represent only a small subset of the spin groups [23], and thus they omit magnetic phases induced by nonrelativistic crystal potentials [7].

The limitations of the magnetic-group formalism can be overcome using the spin-groups formalism, as shown by Šmejkal et al. [7]. This formalism considers pairs of transformations, with the first one acting only on the spin space and the second one on the real space. The resulting symmetry landscape is richer since different transformations can act on the spin and real spaces simultaneously, as compared to the magnetic-symmetry groups where the spin and real space are transformed by the same transformations. The major advantage of this approach is that it offers a systematic description of phenomena and magnetic phases arising from nonrelativistic electromagnetic crystal potentials, which can play a crucial role in magnetism [7].

Šmejkal et al. derived three distinct spin group types to classify all the nonrelativistic collinear magnets into three categories. These are ferromagnets, conventional antiferromagnets with spin-degenerate bands due to the Kramers theorem, and finally, the third distinct phase combining zero net magnetization with spin-split electronic bands that are equally populated [7]. The last category was newly named as *altemagnets*. The difference between the band structure of an altermagnet and a conventional ferromagnet or antiferromagnet is schematically shown in Fig. 1.3.

The altermagnetic spin-splitting originates from a local anisotropic electric crystal field, i. e., from crystal properties of the nonmagnetic phase [7]. Such mechanism contrasts with the conventional ferromagnetic spitting due to the exchange interaction or the spin-orbit splitting. The spin-splitting can induce a variety of magnetism-related phenomena, such as the spontaneous Hall effect that we discuss in the following Chapter 2.

Šmejkal et al. also provided a detailed list of candidate altermagnetic materials including MnO_2, RuO_2, La_2CuO_4, and Mn_5Si_3 [7]. As the last one is of particular interest to this thesis, we shall introduce it in more detail in the following section.

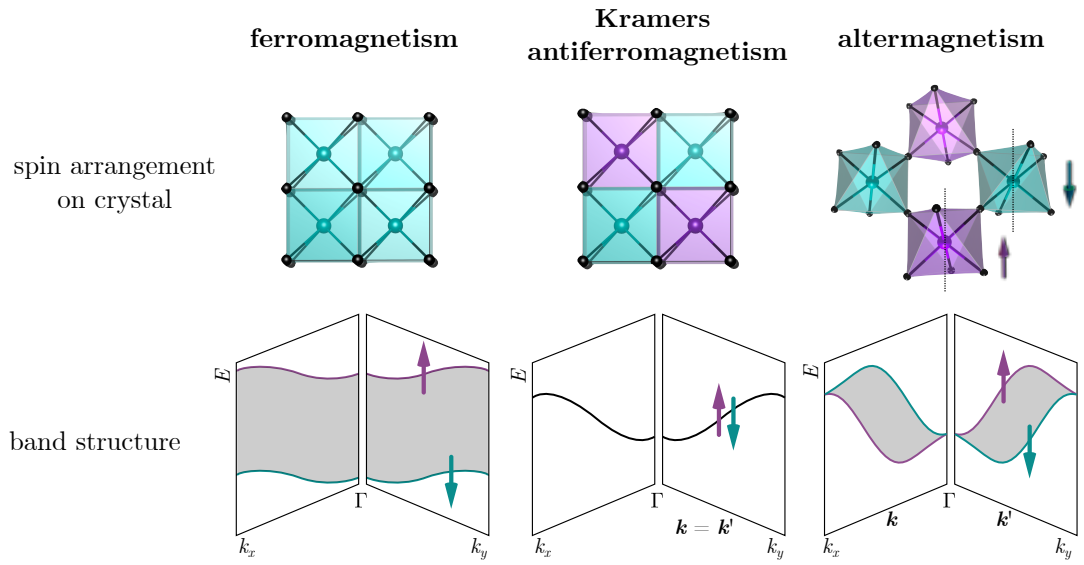

Figure 1.3: Magnetic phases with collinear magnetic order, i. e. ferromagnetic, Kramers spin-degenerate antiferromagnetic, and altermagnetic. **First row**: Illustrative spin arrangements with the opposite spin directions depicted by purple and cyan color. Ferromagnetic and Kramers antiferromagnetic crystal correspond to the structure of FeRh, the altermagnetic crystal to La_2CuO_4. **Second row**: Schematic band structure of ferromagnetically and altermagnetically spin-split bands and a Krammers spin degenerate antiferromagnetic band. Adapted from [7].

1.4 Mn_5Si_3

Mn_5Si_3 is an intermetallic compound that has two distinct antiferromagnetically-ordered magnetic phases, as demonstrated by multiple measurements in poly-crystalline and single-crystal samples [24–31]. Recently, the compound gained considerable scientific attention owing to its interesting thermodynamic (inverse magnetocaloric effect [32]) and transport properties. Particularly, the topological, as well as the spontaneous Hall effect, has been recently observed in thin films of Mn_5Si_3, establishing its magnetic ordering as altermagnetic [24, 28].

Crystal symmetry of the paramagnetic state of Mn_5Si_3 is characterized by the hexagonal space group $P6_3/mcm$, with two distinct crystallographic positions for the Mn atoms (sites $Mn^{(1)}$ and $Mn^{(2)}$) [25]. Neutron scattering in bulk crystals showed that four out of the six $Mn^{(2)}$ sites (see Fig. 1.4) in the unit cell exhibit collinear antiferromagnetic ordering in the temperature range of 70 K to 100 K, with the remaining six manganese and six silicon atoms being nonmagnetic. When decreasing the temperature below 70 K, the crystal symmetry is reduced, establishing a highly noncollinear and noncoplanar arrangement of magnetic spins. In this magnetic phase, also the $Mn^{(1)}$ atoms carry a magnetic moment, yet the two remaining $Mn^{(2)}$ atoms are still without a magnetic moment [25]. The arrangement of magnetic moments in the collinear (cAFM) phase is as shown in

Fig. 1.4a [25, 33–35]. In contrast, the structure of the noncollinear (nAFM) phase is still under debate, and at least three distinct configurations were proposed as in Fig. 1.4b–d.

The transition temperatures to different magnetic states of the material mentioned above were determined on bulk samples and sputtered layers [24]. However, Reichlová et al. observed a substantial shift of the Néel temperature to approximately 240 K for epitaxial layers of Mn_5Si_3 [24]. This enhancement was attributed to the effect of an epitaxial strain that occurs during growth and modifies the structure, as can be seen using temperature-dependent X-ray diffraction.

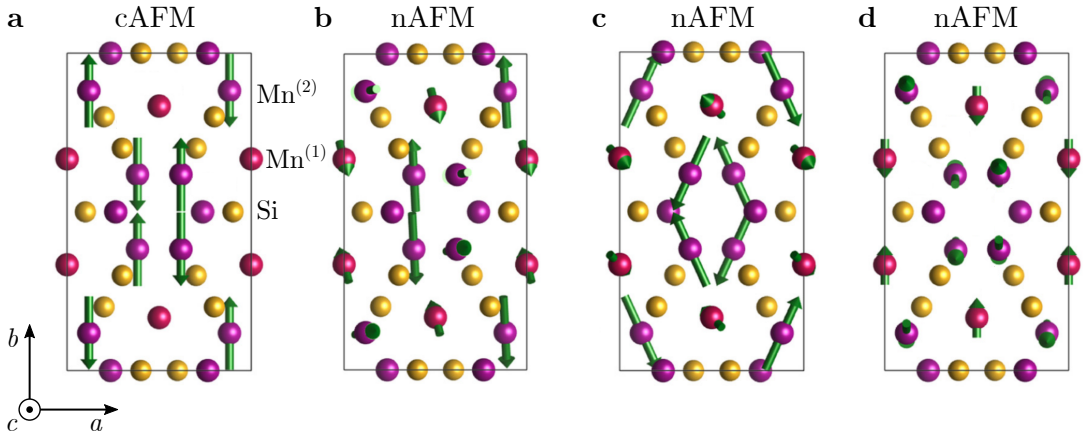

Figure 1.4: Magnetic structure of Mn_5Si_3. Manganese atoms occupy two distinct crystalographic positions $Mn^{(1)}$ (red) and $Mn^{(2)}$ (magenta). **a** Magnetic structure of the collinear antiferromagnetic phase [25, 33–35]. Structure of the noncollinear antiferromagnetic phase according to **b** [36], **c** and **d** [25]. Adapted from [25].

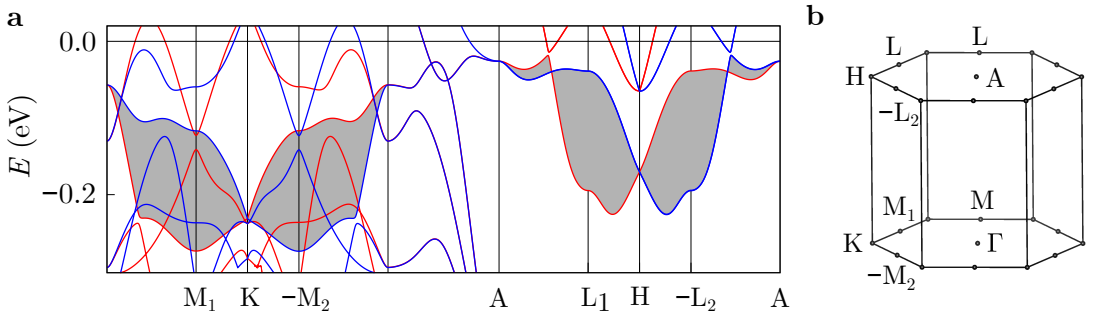

Figure 1.5: Spin-splitting of Mn_5Si_3. **a** Spin-split band structure of Mn_5Si_3 in the $k_z = 0$ plane with relativistic spin-orbit interaction switched off as calculated by Reichlová et al. [24]. **b** The hexagonal Brillouin zone with the notation of high symmetry points. Adapted from [24].

In the same work, the altermagnetic phase of this material was introduced for the first time. Ab-initio calculations of the collinear magnetic phase demonstrated pronounced spin splitting even without the spin–orbit interaction, as shown in Fig. 1.5a [24]. The presence of strong spin splitting in the collinear antiferromagnetic phase suggests that Mn_5Si_3 can represent a prototype altermagnet, in accord with the prediction of the theoretical work [7].

The theoretical prediction of the spin splitting was experimentally confirmed by Reichlová et al. [24] by measurement of the pronounced anomalous Hall conductivity in epitaxial Mn_5Si_3. However, further phenomena that usually accompany spontaneous Hall response, namely the thermotransport and magnetooptical effects, remain yet to be demonstrated. This work aims to explore the thermotransport and magnetooptical response of Mn_5Si_3 thin layers in order to provide a comprehensive picture of the magnetic properties stemming from the altermagnetic ordering of the material.

Chapter 2

Transport properties of Mn_5Si_3

Transport of electric charge is a crucial instrument for studying various properties of solid-state materials. When combined with an external magnetic field, it becomes a major approach for determining fundamental magnetic properties.

This chapter will introduce a link between the transport of electric charge, internal magnetic structure, and symmetries of magnetically ordered materials. Then we describe experimental methods that enable the investigation of this connection. Finally, we present the results of our transport experiments and provide their interpretation in terms of the magnetic structure of Mn_5Si_3.

2.1 Theoretical introduction

2.1.1 Electronic transport, magnetism, and symmetries

When the electric current in any conducting material is exposed to a perpendicular external magnetic field, a transverse voltage is generated (see Fig. 2.1). This phenomenon is the notoriously known Hall effect discovered in 1879 by Edvin Hall, which can be explained by the Lorenz force acting on the charge carriers [37]. We call this effect, which the semi-classical drift-diffusion model can quantitatively describe [38], the ordinary Hall effect (OHE). Two years later — in 1881, Hall reported that the transverse voltage is ten times larger in ferromagnetic iron compared to the non-magnetic conductors. This phenomenon later became the well-known anomalous Hall effect (AHE) [39].

Soon afterwards, it was discovered that the dependence of Hall voltage V_{xy} or Hall resistivity ρ_{xy} on the magnitude of the applied perpendicular field H_z

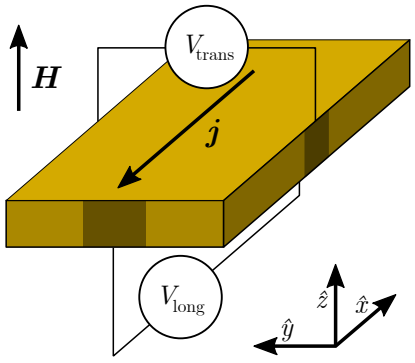

Figure 2.1: Schematic illustration of the ordinary Hall effect induced by the external magnetic field $\mu_0 \boldsymbol{H}$ and the current $\boldsymbol{j}$.

qualitatively differs for magnetic and non-magnetic materials: While the OHE shows a linear dependence on H_z, ferromagnetic materials evince a linear behaviour of ρ_{xy} in the weak fields and saturation at higher fields (see Fig. 2.2). The saturation field H_z is roughly proportional to the component of magnetization M_z [17]. Later, an empirical relation for the transverse resistivity was established:

$$\rho_{xy} = R_0 H_z + R_s M_z, \tag{2.1}$$

where the first term is equivalent to the ordinary and the second to the anomalous Hall effect, with the corresponding coefficients R_0 and R_s [40].

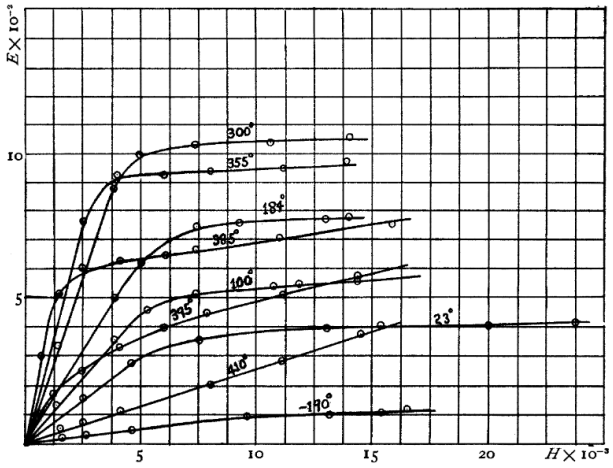

Figure 2.2: (Anomalous) Hall effect in nickel. Temperature is given in °C. Adapted from [41].

Despite this phenomenological relationship, a microscopic theory of AHE turned out to be particularly difficult to formulate. The first such theory was proposed in 1954 by Karplus and Luttinger, who showed that electrons in solids acquire additional, transverse contributions to the group velocity under an external electric field. The sum of these contributions (called *anomalous*) is non-zero for ferromagnetic conductors [42]. Although this theory underwent severe disputes in the following decades, the idea of anomalous velocity was eventually generalized by the concept of Berry's phase and the Berry curvature, which became crucial for the microscopic understanding of the anomalous Hall effect [17].

Berry's phase is an additional phase of an electron's wavefunction arising in systems with multiple time-dependent parameters in the Hamiltonian. The Berry curvature is then a vector field in the space of the time-dependent parameters, with Berry's phase being its integral over a closed trajectory [43]. Although we will not introduce these terms in more detail, we shall note two important properties of the momentum-space Berry curvature: Firstly, it is directly proportional to the anomalous Hall conductivity, and secondly, the Berry curvature can be only non-zero when the combined time-reversal ($\mathcal{T}$) and mirror reflection symmetry is broken [16].

Let us now briefly focus on the relationship between the symmetries of a physical system and its response to an external stimulus, as such considerations play a crucial role in explaining modern transport phenomena. An important relation between the response $K_{\alpha\beta}(\omega, b)$ of a physical quantity α to a stimulus connected with the quantity β was formulated by Onsager [44]:

$$K_{\alpha\beta}(B) = \varepsilon_\alpha \varepsilon_\beta K_{\beta\alpha}(-B), \tag{2.2}$$

where $\varepsilon_{\alpha,\beta} = \pm 1$ specifies the symmetry property of α and β with respect to the operation of time-reversal. B is any $\mathcal{T}$ breaking field, e.g. in the case of a ferromagnet, B can be associated with magnetization. Now, we shall apply this theorem to a conductivity tensor σ_{ij} and the current response function, i.e. $\alpha \to J_i$ and $\beta \to J_j$, where $J_{i,j}$ are components of a current density vector. The charge current is odd under the $\mathcal{T}$ symmetry and thus $\varepsilon_{\alpha,\beta} = -1$. From Eq. (2.2) it holds that:

$$\sigma_{ij}(B) = \sigma_{ji}(-B). \tag{2.3}$$

As a consequence, the conductivity tensor is symmetric when no $\mathcal{T}$ symmetry breaking field is present, i.e. $\sigma_{ij}(B = 0) - \sigma_{ji}(-B = 0) = 0$. The antisymmetric part $\sigma_{ij}(B) - \sigma_{ji}(B)$ can be finite *only* if the $\mathcal{T}$ symmetry is broken [17]. This is a valuable tool for confirming the $\mathcal{T}$ symmetry of solids, since the measurement of σ_{ij} properties is straightforward.

A simple example of a $\mathcal{T}$-symmetry-breaking field can be an external magnetic field in conductive solids. The drift-diffusion model yields that $\sigma_{xy}(B)$ - $\sigma_{yx}(B) = 2 \cdot \sigma_{xy}(B) \neq 0$ when magnetic field is applied along the z-axis. This can be observed as the ordinary Hall effect.

As already stated, the magnetic field in a solid — either external or internal — breaks the time-reversal symmetry. However, recently, new mechanisms of the $\mathcal{T}$ symmetry breaking were proposed, resulting in new types of the Hall effect (such as the topological Hall effect) or the presence of the AHE in materials with zero net magnetic moment (in noncollinear antiferromagnets). We shall now introduce these phenomena as their understanding is crucial for our experimental observations.

Anomalous Hall effect in antiferromagnets From the empirical expression (2.1), it may be assumed that the anomalous Hall effect in a particular material is proportional to its magnetization. Although no microscopically justified relationship was established, the proportionality (though not necessarily linear) was expected till recently [16]. However, in 2014 Chen et al. [16] pointed out that a finite anomalous Hall response can be present even in a noncollinear antiferromagnet with zero net magnetization when certain common symmetries are absent. This was shown for Mn_3Ir with a kagome lattice of magnetic Mn atoms. Magnitude of the resulting AHE is comparable in size to AHE in the elemental transition metal ferromagnets (e.g. iron). Up to now, the AHE has been experimentally identified in several noncollinear antiferromagnets Mn_3X for X being Sn [45], Ge [46], Ga [47], and other noncollinear systems.

In contrast, breaking of the $\mathcal{T}$ symmetry in collinear antiferromagnets and consequent Hall conductivity has not been reported [48]. However, a 2020 work by Šmejkal et al. [48] suggested a new mechanism of the $\mathcal{T}$ symmetry breaking even in antiferromagnets with collinear spin structure, so called altermagnets (for the details about altermagnetism and its origin, see Sec. 1.3). The terminology for the resulting Hall effect is not settled yet and either the term *crystal Hall effect* [48], *anomalous Hall effect* [24], or simply *spontaneous Hall effect* is used.

Topological Hall effect In ferromagnets and antiferromagnets with topologically nontrivial spin texture, another mechanism of the $\mathcal{T}$ symmetry breaking was

proposed, resulting in the topological Hall effect (THE) [49]. In ordered materials where the spins in the individual sublattices are not parallel to each other, it is convenient to introduce the spin chirality $\kappa = \sum \boldsymbol{S}_i \cdot (\boldsymbol{S}_k \times \boldsymbol{S}_l)$ with $\boldsymbol{S}_{i,k,l}$ being three magnetic moments in the magnetic lattice. Note that for collinear ordering, κ is identically zero. A finite spin chirality can induce a real-space Berry curvature and, consequently, also the THE. In contrast to the anomalous Hall effect, the THE can thus manifest even without the spin-orbit interaction [28].

So far, the THE has been observed in various systems, including double-exchange ferromagnets [50], the noncollinear antiferromagnet Mn_3Sn [51], and also in the noncollinear phase of the antiferromagnet Mn_5Si_3 [28].

Magnetoresistance The effect of the Lorenz force acting on charge carriers in a conductor can be observed as a transverse voltage, but it also leads to an increase of longitudinal resistivity ρ_{xx} as a consequence of the charge carriers being deflected. This effect is called ordinary magnetoresistance (OMR) and is usually described by the ratio:

$$MR = \frac{\rho_{xx}(H) - \rho_{xx}(H=0)}{\rho_{xx}(H=0)}, \tag{2.4}$$

which for OMR follows a quadratic dependence on H [52].

In ferromagnets, an additional mechanism links longitudinal resistivity with magnetism. This is anisotropic magnetoresistance (AMR) which manifests as an anisotropic change of resistivity due to the non-zero magnetization $\boldsymbol{M}$: When $\boldsymbol{M}$ is parallel to the electric current, longitudinal resistivity is $\rho_{||}$. However, when magnetization and current are perpendicular to each other, it becomes $\rho_{\perp}$. AMR is then described by the difference $\rho_{||} - \rho_{\perp}$.

According to the recent observations, anisotropic magnetoresistance is not only limited to ferromagnets, and it was already observed in antiferromagnetic compounds such as Sr_2IrO_4 [53].

2.1.2 Thermoelectric transport

The Hall effect and other conventional magnetotransport phenomena are driven by a mechanical force, i.e., an electric field, which can be described at a microscopic level as a perturbation to the Hamiltonian. However, there is also another kind of transport — transport that is induced by a statistical force, e.g., by a gradient of temperature or chemical potential that is defined only through the statistical distribution of the carriers. An example of the latter kind is thermoelectric phenomena that connect a thermal stimulus (heat flow) and an electric response (electric field) [54].

This kind of the charge transport can be viewed as a direct counterpart of the electronic transport described in the previous section: the ordinary Nernst effect (ONE), like the ordinary Hall effect, manifests as a transverse voltage in the presence of a perpendicular magnetic field. However, in this case, the effect is induced by a longitudinal temperature gradient rather than by longitudinal electric current.

The ONE is characterized by the Nernst coefficient N as follows:

$$E_y = N\, B_z\, \partial T/\partial x, \tag{2.5}$$

where E_y is the transverse electric field, $\partial T/\partial x$ is a longitudinal temperature gradient, and B_z is the out-of-plane magnetic field (see Fig. 2.3). There are also other thermoelectric effects in the magnetic field that manifest, for example, as a conversion of the longitudinal electric current to the transverse temperature gradient (the Ettingshausen effect) or as a conversion of the longitudinal heat flow to the transverse temperature gradient (the Righi-Leduc effect) [55]. However, these phenomena are not relevant to this thesis.

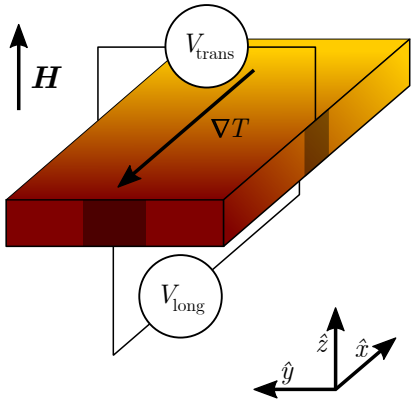

Figure 2.3: Schematic illustration of the ordinary Nernst effect induced by the external magnetic field $\mu_0 \boldsymbol{H}$ and the temperature gradient ∇T.

Although fundamentally different forces drive the electric and thermoelectric transport phenomena, there is a substantial link between the electric conductivity tensor $\overline{\sigma}$ and the thermoelectric tensor $\overline{\alpha}$.

The charge current $\boldsymbol{J_e}$ and the heat current $\boldsymbol{J_q}$ can be described by the following set of two equations:

$$\boldsymbol{J_e} = \overline{\sigma}\,\boldsymbol{E} - \overline{\alpha}\,\nabla T, \tag{2.6}$$

$$\boldsymbol{J_q} = T\,\overline{\alpha}\,\boldsymbol{E} - \overline{\kappa}\,\nabla T, \tag{2.7}$$

where $\overline{\kappa}$ is the thermal conductivity tensor, $\boldsymbol{E}$ is electric field, and ∇T is a gradient of temperature. Considering a Fermi-Dirac distribution of charge carriers and a low-temperature limit, a connection between $\overline{\alpha}$ and $\overline{\sigma}$ arises. This link is called the Mott relation:

$$\overline{\alpha} = \frac{\pi^2}{3}\frac{k_B^2\,T}{e}\left.\frac{\partial\,\overline{\sigma}}{\partial\,\epsilon}\right|_{\epsilon=\epsilon_F}, \tag{2.8}$$

where ϵ is energy of the carriers (ϵ_F is the Fermi energy) and T is temperature [54, 56].

The Nernst coefficient N mentioned above relates to α_{xy} in the limit of weak magnetic fields as follows [56]:

$$N = B_z\,\frac{\alpha_{xy}}{\sigma_{xx}}, \tag{2.9}$$

The Mott relation then connects the off-diagonal elements of the $\overline{\alpha}$ and $\overline{\sigma}$ tensors, which in the presence of an external magnetic field creates a link between the ordinary Nernst and Hall effects.

Anomalous Nernst effect Besides the ordinary Nernst effect, there is also a thermoelectric counterpart to the anomalous Hall effect: the anomalous Nernst effect (ANE). Applying a temperature gradient in a ferromagnet generates a voltage

that is perpendicular to both the heat flow and the magnetization. This is the phenomenological description of the anomalous Nernst effect that holds for ferromagnets with a finite net magnetization. However, the natural question is whether the mechanism of the Berry phase, which causes the AHE, also manifests in transport driven by a statistical force. In other words, whether the Mott relation (2.8) also holds for the anomalous contribution to σ_{xy} and α_{xy}. In ferromagnets, it is already known that the relation remains unchanged [54]. However, there are theoretical concerns about the validity of the Mott relations in materials with a nontrivial topology of the electronic bands, and it was proposed that the ANE could be sensitive to the electronic states invisible to the AHE [57]. This assumption remains yet to be confirmed; however, the ANE has already been observed in noncollinear antiferromagnetic compounds, for example, in Mn_3Sn [58].

Thermal magnetoresistance Since the conductivity tensor is connected to the thermoelectric tensor through the Mott relations, the longitudinal components of the thermoelectric tensor α_{xx} can be generally dependent on the magnetic field similarly to ρ_{xx}. This gives rise to the thermoelectric counterpart of OMR, ordinary thermal magnetoresistance. Ferromagnets and other magnetically ordered materials then show anisotropic thermal magnetoresistance (ATMR), which is the thermal counterpart of AMR [59].

2.2 Samples and transport methods

2.2.1 Samples

In order to measure both electronic-transport and thermoelectric-transport properties of Mn_5Si_3, we used a Mn_5Si_3 thin-film grown at the Interdisciplinary Center of Nanoscience of Marseille by our collaborating group. The sample consists of a 17-nm thick layer of Mn_5Si_3, grown on an intrinsic silicon (111) substrate using molecular-beam epitaxy. On the interface between silicon and Mn_5Si_3, there was also an additional MnSi phase of 4 % that facilitated good crystallinity of the thin film.

The sample was lithographically patterned by our collaborating group at Spintec in Grenoble in two steps: The first step consisted of patterning the Mn_5Si_3 layer using electron-beam lithography and ion-beam etching. Consequently, a lift-off profile was patterned. A 10-nm platinum layer was deposited by magnetron sputtering, and excessive platinum was removed by lift-off. Unfortunately, the platinum lift-off was not entirely successful, as shown in Fig. 2.4d where the dotted curves mark the damaged and discontinuous platinum layer.

There are three types of structures that were lithographically patterned, as shown in Fig. 2.4a–c: The design **a** was intended for the thermoelectric measurement, as it consisted of a Mn_5Si_3 Hall bar and multiple platinum contacts used for heating and thermometry. The designs **b** and **c** were purely Mn_5Si_3-based.

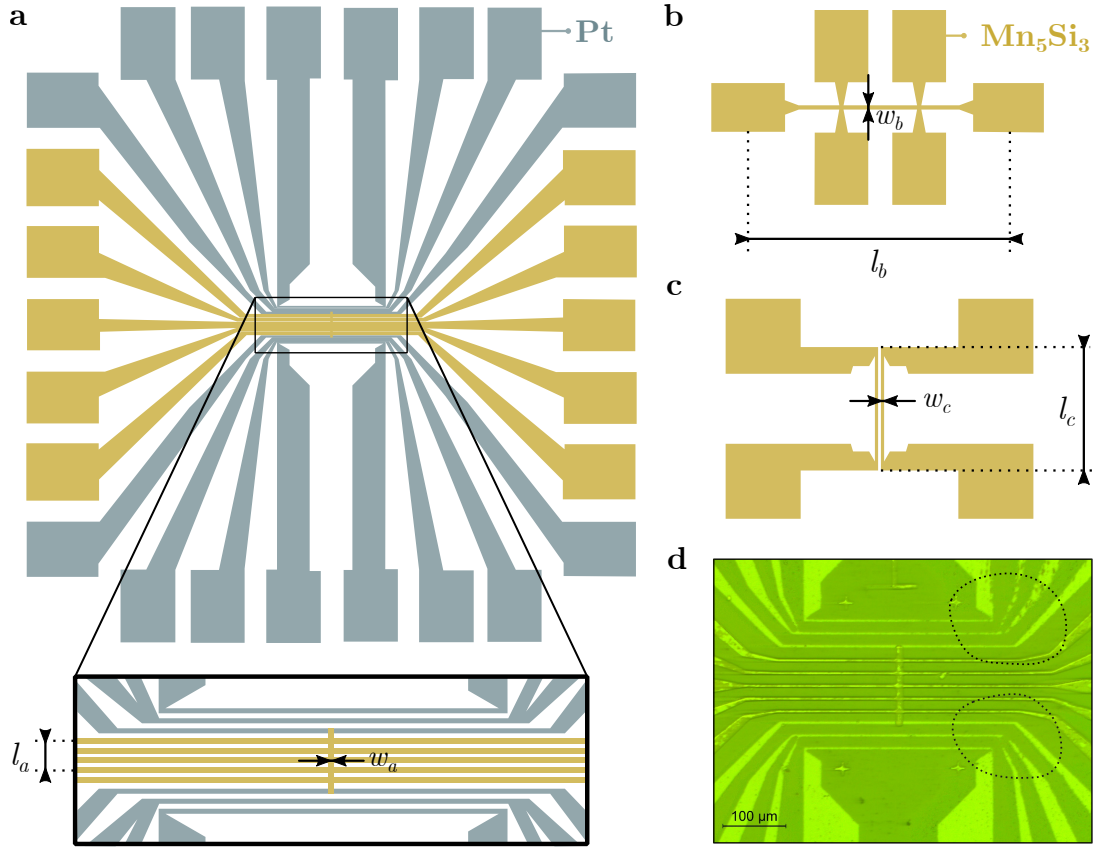

Figure 2.4: **a**, **b**, **c** Designs of devices for transport measurements. **d** Microscopic image of the device a with dotted curves showing the damages of the platinum layer. The dimensions of the devices are following: $w_a = 10\,\mu$m, $w_b = 8\,\mu$m, $w_c = 5\,\mu$m, $l_a = 30\,\mu$m, $l_b = 760\,\mu$m, $l_c = 340\,\mu$m.

2.2.2 Measurement of electronic transport in magnetic field

A magnetotransport experiment is based on measuring components of the resistivity tensor while stimulating the system with an external magnetic field. Mn_5Si_3 shows magnetic order only at low temperatures below 240 K (see Sec. 1.4). The measurement was therefore performed in a continuous-flow helium cryostat *Oxford Instruments*, equipped with a vector superconducting electromagnet with a maximum field of 6 T in the z-axis and 2 T in the x- and y-axes (see Fig. 2.5 for the definition of the coordinate system).

For the electronic-transport measurement, a device from Fig. 2.4a was used as illustrated on a measurement scheme in Fig. 2.5. Longitudinal electric current along the x-axis was induced by a current source *Keithley SourceMeter 2450* while measuring transverse and longitudinal voltage V_{xy} and V_{xx} using nanovoltmeters *Keithley 2182A*. In order to eliminate any signal independent of the current polarity (e.g. thermal effects), the *gradient reversal technique* was employed (see [60]): every data point was obtained by subtracting signals measured with opposite polarities of the longitudinal current. During the experiment, the magnitude of the external magnetic field of a fixed direction was changed — we shall call this kind of experiment a *field sweep*.

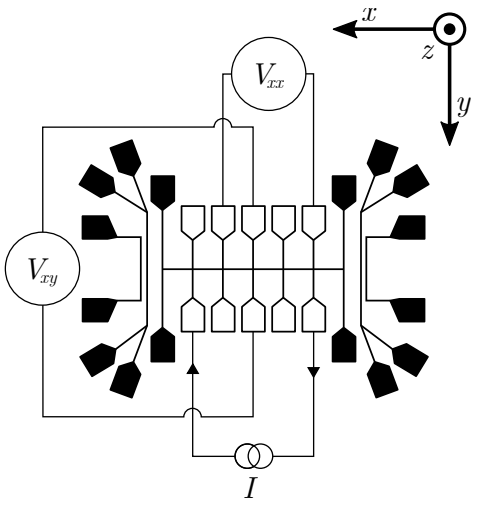

Figure 2.5: Measurement of electric transport in magnetic field. Longitudinal electronic current is induced by a current source I while measuring transverse voltage V_{xy} and longitudinal voltage V_{xx}.

2.2.3 Measurement of thermoelectric transport

Measurement of thermoelectric properties was performed using the same experimental setup and the same sample as for the electronic-transport experiments. However, in a thermoelectric experiment, it is necessary to induce a well defined longitudinal temperature gradient. This is a nontrivial problem compared to the current flow induced by a current source in the electronic-transport experiment.

We used two methods of generating the temperature gradient. The first one, illustrated in Fig. 2.6a, uses a device with platinum contacts (see Fig. 2.4a). The source of an in-plane temperature gradient is one pair of platinum contacts connected to a current source I_H *Keithley SourceMeter 2450*. The Joule heat generated by the platinum stripe then spreads, creating a temperature gradient along the x-axis over the Hall bar located between the heater contacts. The Hall bar serves for the measurement of longitudinal V_{xx} and transverse V_{xy} voltage, generated by the temperature gradient. Both voltages were measured by the *Keithley 2182A* nanovoltmeters. The heating power was 83 mW. Although this measurement technique is well established [61], we did not manage to obtain any reasonable signal when measuring a sweep of the out-of-plane magnetic field. This was supposedly caused by the poor quality of the platinum layer (as illustrated in Fig. 2.4d), resulting in no temperature gradient. We, therefore, moved to the second method, where external heaters generated the temperature gradient.

The second method is shown in Fig. 2.6b: The sample itself does not lie directly on the chip carrier as in a standard electronic-transport measurement but is supported by two columns. The column on the "hot" side of the sample (on Fig. 2.6 in red) consists of a platinum resistor Pt2000 and a supporting plastic (ASA) block. The second column on the "cold" side (yellow) contains a Pt2000 resistor and a brass block. The Pt2000 are flat-shaped platinum resistors of the resistance of 2 kΩ. The resistor on the "hot" side is used as a heater, whereas the second one serves only for thermometry. The power on the heater was up to 2.1 W. The ASA block is a good thermal insulator, and so the majority of the generated heat is conducted away through the sample and then through the brass block to the chip carrier (see white arrows in Fig. 2.6b).

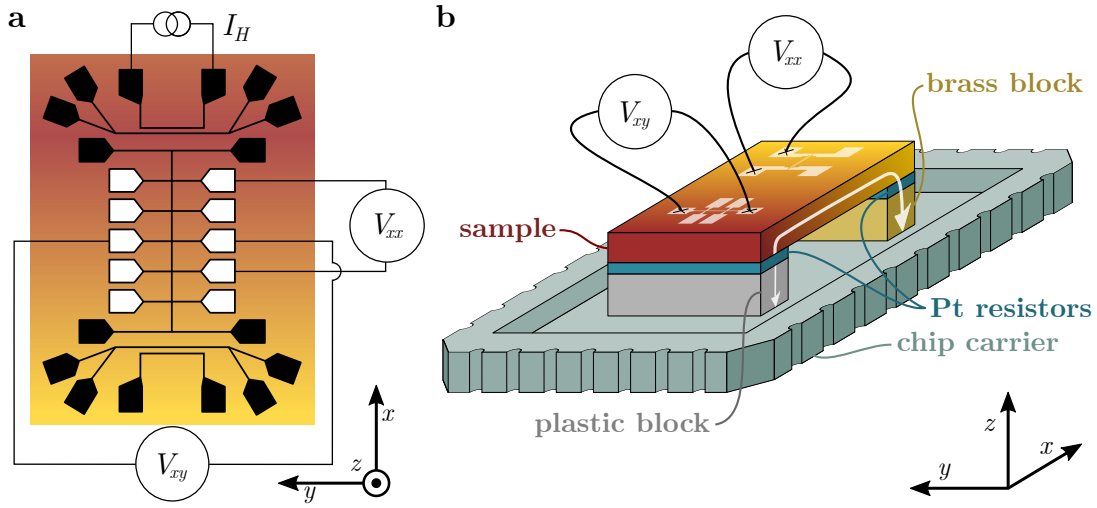

Figure 2.6: Measurement of thermoelectric transport in the magnetic field. **a** A method of generating longitudinal temperature gradient using on-chip platinum heaters. **b** An alternative method where an external platinum resistor (glued to a plastic block) generates a heat flow along with the sample, which is absorbed in the chip carrier through a brass block.

The advantages of this configuration are the following: The Pt2000 can be loaded by a substantially higher power than the on-chip heaters, where the Pt layer is only 10 nm thick. This results in a substantially larger temperature gradient and better signal-to-noise ratio since the large currents densities in on-chip heaters are an additional noise source. In addition, the heat is conducted mainly through the sample compared to the sample glued directly on the chip carrier, which transfers the heat directly away from the sample.

Generated thermovoltage was detected separately on two different devices: longitudinal voltage V_{xx} was measured on the device in Fig. 2.4c, and the transverse voltage V_{xy} on the device in Fig. 2.4b, both of them using the *Keithley 2182A* nanovoltmeters. These devices were chosen because their longitudinal/transverse dimension was the largest available, allowing them to collect as much thermovoltage as possible. There were no platinum contacts that could be used for thermometry in this measurement.

Being able to measure temperature $T_{A,B}$ in two points along the temperature gradient is crucial for the calibration of the temperature gradient. Under the usual assumption that the gradient is linear, its magnitude can be calculated as:

$$|\nabla T| = \frac{T_A - T_B}{l}, \tag{2.10}$$

where l is the separation distance between the points A and B.

Because no platinum thermometers were used in this experiment, we were forced to use the Mn_5Si_3 contacts for the thermometry in the following way: Firstly, we measured the temperature dependence of the resistivity (see Fig. 2.7) for two transverse contacts separated by a distance l. Then we applied a longitudinal temperature gradient, measured the resistivities of these contacts and correlated them with the temperature dependence. We would also follow the same procedure

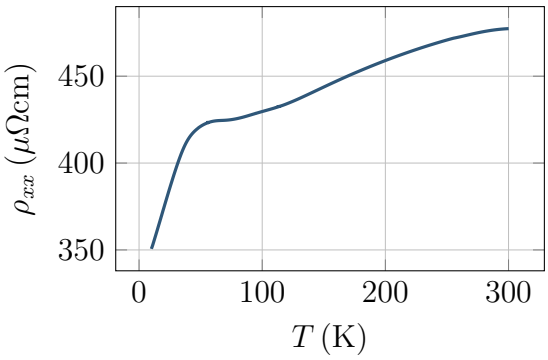

Figure 2.7: Temperature dependence of resistivity of Mn_5Si_3.

for platinum contacts; however, the resistivity of Mn_5Si_3 is much less dependent on temperature than the resistivity of platinum which dramatically decreases the precision of such calibration. Another complication is that the temperature dependence of resistivity of Mn_5Si_3 is not monotone and several temperatures yield the same resistance values (see Fig. 2.7). However, this can be partially eliminated since we simultaneously measure the resistance on both Pt2000 resistors, which gives us a lower and an upper limit for the temperatures at each side of the device.

Using this approach, we arrived at the estimate of the temperature gradient magnitude, which was, depending on the measurement, between 0.1 K mm^{-1} and 2 K mm^{-1}. However, we should stress that these values are only approximate and not reliable enough to be used for precise estimation of the Nernst coefficient.

2.3 Experimental results

In our investigation of the Mn_5Si_3 transport properties, we build upon our previous extensive study of multiple samples of Mn_5Si_3 thin films with different crystalline quality [60]. In this work, we focus on a deeper analysis of the transport data and mainly on their relation to the thermotransport experiments.

2.3.1 Electronic transport

In order to first understand the behaviour of the Hall signal in the studied sample, we performed field sweeps in the z-direction. The external magnetic field was swept between ±6 T with a ramping rate of 0.5 T/min. We applied longitudinal electric current of $I = 100$ μA while measuring longitudinal and transverse voltage V_{xx} and V_{xy}. The sweeps were done at various temperatures ranging from 5 K to 250 K.

Voltages V_{xx} and V_{xy} were used to calculate longitudinal and transverse resistivities ρ_{xx} and ρ_{xy} which were a basis for our further analysis. The signals were then subject to further processing to reveal particular features in the measured field dependencies. In the ideal geometry of the Hall bar contacts, the longitudinal voltage should show only effects connected with longitudinal resistance components, and the same should hold for transverse voltage and resistivity. However, as our contacts were not ideal due to the finite width w and imperfect alignment, there was always a finite projection of ρ_{xx} and ρ_{xy} to the transverse and longitudinal voltages. This effect, which can be substantial, is usually suppressed by symmetrization of the longitudinal resistivity and antisymmetrization of the

transverse resistivity with respect to the external magnetic field. This is justified by the usual assumption that transverse resistivity is an odd function of the external magnetic field, whereas longitudinal resistivity is even in the magnetic field [62]. This is a reasonable assumption for the dominant signals resulting from the anomalous Hall effect or the topological Hall effect, and we use this approach for most of our presented data. However, we also revealed that certain types of magnetotransport signals do not obey this assumption. Therefore, we invented a novel approach for data analysis that enables the separation of an intrinsic symmetric contribution to the transverse signal.

Let us now focus on the analysis of the individual signals separately, i.e., longitudinal resistivity ρ_{xx} and transverse resistivity ρ_{xy}.

Longitudinal resistivity Longitudinal resistivity ρ_{xx} was calculated from the corresponding voltage using the formula:

$$\rho_{xx} = \frac{V_{xx}}{I} \frac{t\,w}{l}, \tag{2.11}$$

where t is the thickness of the Mn_5Si_3 layer, and w and l are dimensions of the device as stated in Sec. 2.2.1. The field dependence of ρ_{xx} was then symmetrized with respect to the external magnetic field $\mu_0 H_z$. The resulting symmetrized signals are shown in Fig. 2.8: In a figure **a**, there is the field dependence of the longitudinal resistance for several temperatures. The corresponding signals are offset to zero as $\Delta\rho_{xx}(H_z) = \rho_{xx}(H_z) - \rho_{xx}(0)$. The quantity $\Delta\rho_{xx}(H_z)$ is used instead of the as-measured ρ_{xx} to stress the difference in the magnetic field dependence of longitudinal resistivity at different temperatures. Fig. 2.8b shows more details of the ρ_{xx} close to 150 K where the signal changes sign. Finally, in Fig. 2.8c, the temperature dependence of magnetoresistance measured at 5 T is depicted, which was calculated from the longitudinal resistance as follows:

$$MR = \frac{\rho_{xx}(5\text{ T}) - \rho_{xx}(0\text{ T})}{\rho_{xx}(0\text{ T})}. \tag{2.12}$$

As apparent from Fig. 2.8a, the magnetoresistance is negative under 150 K, then it crosses zero and becomes positive. This complies with our previous observations in Mn_5Si_3 [60]. However, in the current experiment, the transition is revealed with better resolution in temperature. There is also a clear change in the signal shape between 110 K and 130 K, not correlated with the phase transition temperature — see Fig. 2.8. We interpret this particular change in shape as a competition of at least two components with different temperature dependence: the negative contribution dominates below 150 K while the positive is stronger at higher temperatures, and at around 150 K, the contributions equalize. One possible explanation of these two signals is that (negative) magnetoresistance originating in the antiferromagnetic ordering becomes weak when approaching the transition to the paramagnetic regime, where ordinary magnetoresistance (which is always positive) starts to dominate. However, a deeper understanding of the underlying physics is needed to attribute these signals to particular physical phenomena.

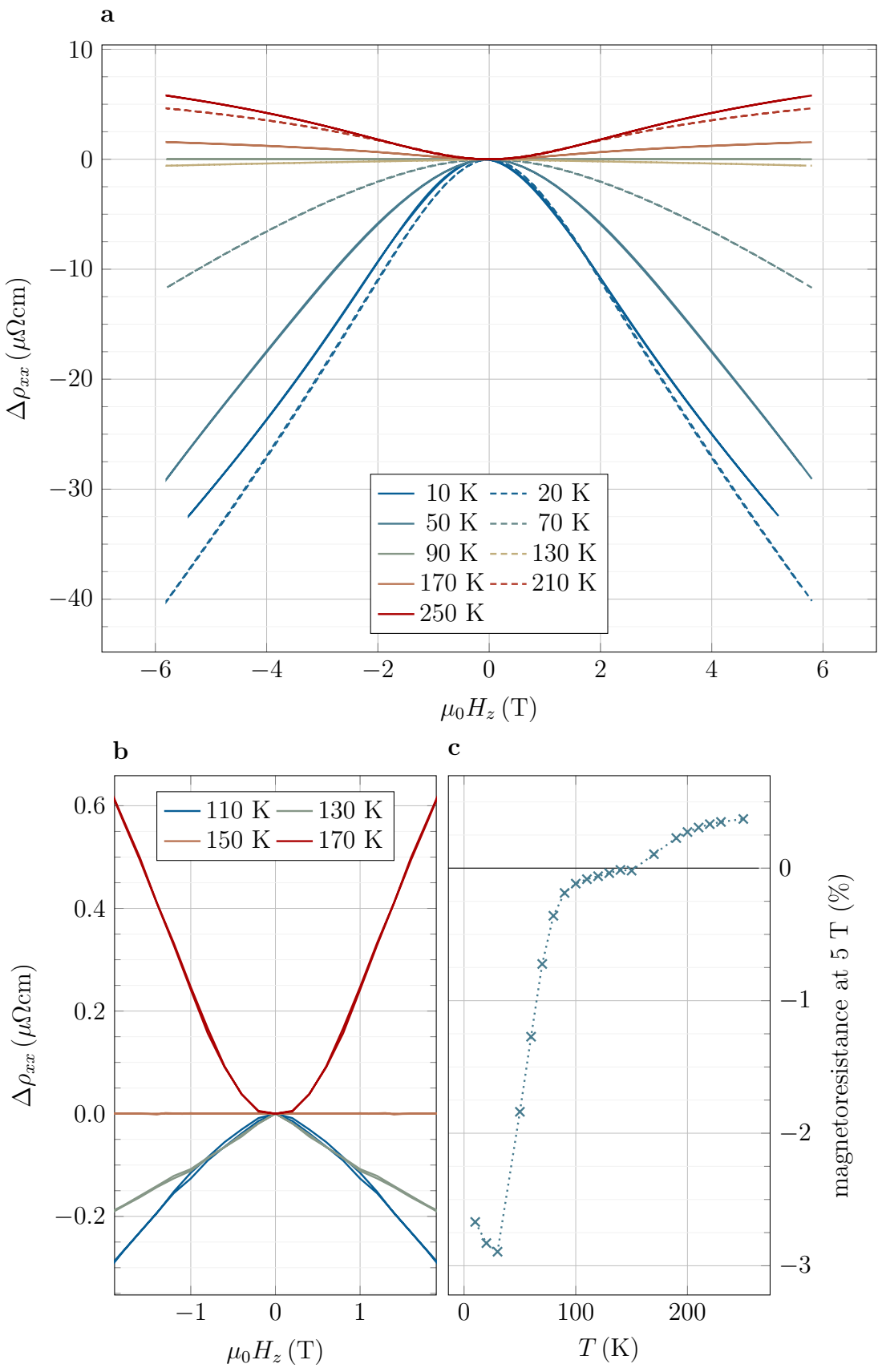

Figure 2.8: Longitudinal resistivity $\Delta\rho_{xx}$. **a** $\Delta\rho_{xx}$ as a function of the applied out-of-plane external magnetic field H_z measured at multiple temperatures. **b** Detail of the field sweeps for temperatures around 150 K. **c** Temperature dependence of magnetoresistance ratio at 5 T.

Transverse resistivity For our further analysis, the transverse signal will play the main role. The expression for calculating the transverse resistivity from the measured voltage V_{xy} is analogous to the recalculation of the longitudinal signal in Eq. (2.11):

$$\rho_{xy} = \frac{V_{xy}}{I}\,\frac{t\,w}{w} = \frac{V_{xy}}{I}\,t, \tag{2.13}$$

where t is the thickness of the Mn_5Si_3 layer, and w and l are dimensions of the device as stated in Sec. 2.2.1.

An example of the raw $\rho_{xy}(H_z)$ field-sweep data measured at 30 K is shown in Fig. 2.9a. Obviously, the dependence is not a square-shaped hysteresis loop, typical for simple ferromagnets. Therefore, it was necessary to modify the standard approach to analyzing the data. As the Hall effect is an odd function of the magnetic field, we were primarily interested in studying the purely antisymmetric component of ρ_{xy} with respect to H_z. The first natural step was the antisymmetrization of the data, as shown in Fig. 2.9b. In addition, there is a substantial linear contribution corresponding to the ordinary Hall effect (see Sec. 2.1.1) that had to be removed. The corrected loops, after the OHE subtraction, are shown in Fig. 2.9c.

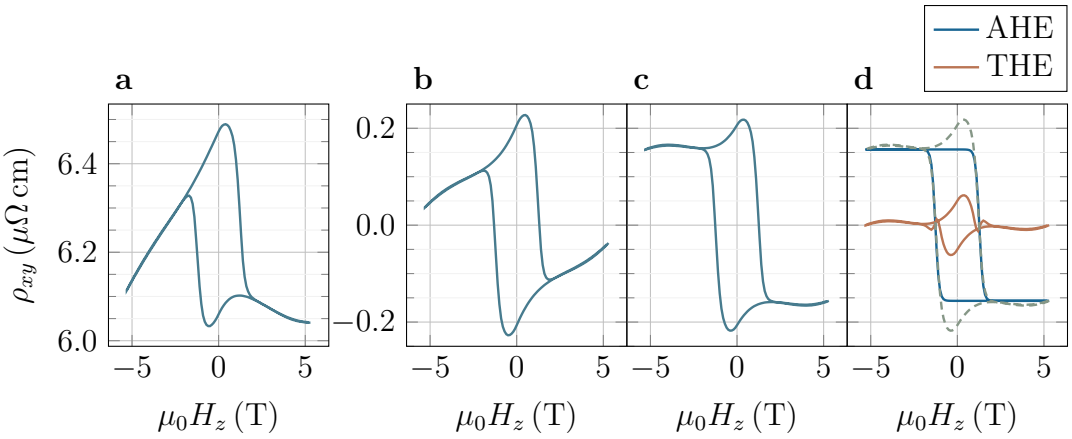

Figure 2.9: Analysis of the ρ_{xy} data, as shown on an example of field sweeps measured at 30 K. **a** Raw ρ_{xy} data. **b** Antisymmetrized ρ_{xy}. **c** Antisymmetrized ρ_{xy} with a linear background removed. **d** Processed ρ_{xy} (dashed line) can be decomposed into a rectangular hysteresis loop (blue) corresponding to AHE and into the THE contribution (orange).

However, even after the standard data processing, the curves do not resemble a typical square-shaped hysteresis loop. There is a substantial contribution of the topological Hall effect, which manifests as a "bump" in the vicinity of zero field [24]. In order to decompose the curve into a component corresponding to the THE and a rectangular hysteresis loop which arises due to the anomalous (spontaneous) Hall effect, we fitted the data in Fig. 2.9c by a pair hyperbolic tangent functions [24]. This procedure is illustrated in Fig. 2.9d where both the original data and the particular components are shown. Note that this approach is only a phenomenological description, with no particular physical model of the system in mind.

As already mentioned, the antisymmetrization of the transverse signal is a usual procedure [24]. It is motivated by the assumption that there may be an

additional contribution due to the contact misalignment, typical for any transport measurement on lithographic structures. This artefact is symmetric with respect to the applied magnetic field, as it is a projection of the (symmetric) longitudinal signal. By the antisymmetrization, we remove this contribution. However, any nontrivial symmetric components that do not originate in the contact misalignment are inherently removed by this procedure. Here, we introduce a method of extracting such intrinsic symmetric component $\rho_\perp$. The formula which introduces $\rho_\perp$ can be written as follows:

$$\rho_\perp = \rho_{xy}^{\mathrm{sym}} - \frac{\mathrm{mean}\left(\rho_{xy}^{\mathrm{sym}}\right)}{\mathrm{mean}\left(\rho_{xx}^{\mathrm{sym}}\right)} \cdot \rho_{xx}^{\mathrm{sym}}, \tag{2.14}$$

where ρ_{xx}^{sym} and ρ_{xy}^{sym} are symmetrized components of longitudinal and transverse resistivities. By Eq. (2.14), we scale the (symmetric) longitudinal signal to the magnitude of the symmetric transverse signal, and then subtract this projection from symmetrized transverse resistance. The resulting $\rho_\perp$ can be attributed to an intrinsic symmetric contribution to the off-diagonal component of the conductivity tensor.

The extraction of $\rho_\perp$ is illustrated in Fig. 2.10: The raw data (panel **a**) is decomposed into its symmetric component in **b**. Fig. 2.10c then shows $\rho_\perp$.

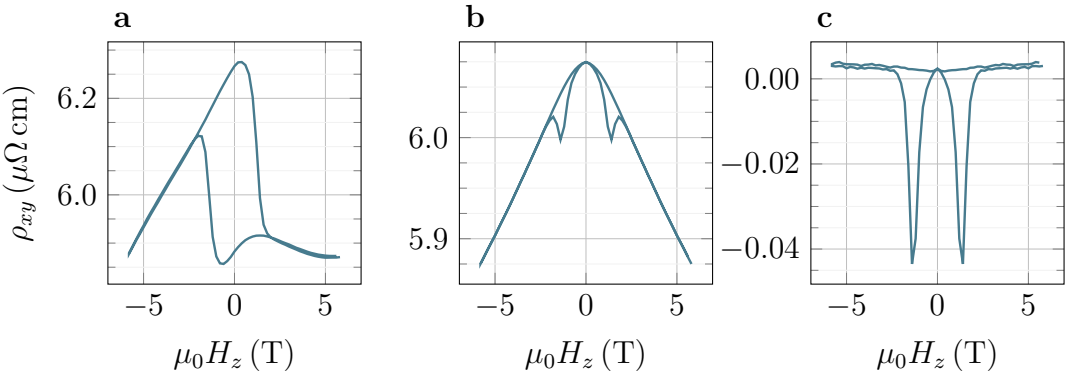

Figure 2.10: Symmetric component of ρ_{xy}. **a** Raw transverse resistivity as measured during a field sweep at 20 K. **b** Symmetric component of $\rho_{xy}\,(H_z)$. **c** $\rho_\perp\,(H_z)$ determined using Eq. (2.14).

The above-described analysis enables us to decompose the transverse signal into multiple components: the contributions of the anomalous Hall effect, the topological Hall effect, and the intrinsic symmetric component $\rho_\perp$. These contributions are depicted in Fig. 2.11: Figure **a** shows the processed $\rho_{xy}\,(H_z)$ dependence (linear background removed and antisymmetrized) for multiple temperatures. In Fig. 2.11b, the temperature dependence of the magnitude of the topological contribution to ρ_{xy} is displayed, while in Fig. 2.11c, we show the temperature dependence of the $\rho_\perp$ magnitude. Please note that the measurement at 30 K does not follow the overall trend of $\rho_\perp$, and the $\rho_\perp$ magnitude drops to zero.

From the signals in Fig. 2.11, it is apparent that the transverse resistivity evinces a clear hysteretic behaviour in the entire studied temperature region. The coercive field has a non-monotone dependence on temperature, with a minimum value close to 100 K and a substantial increase above 200 K (for a detailed analysis

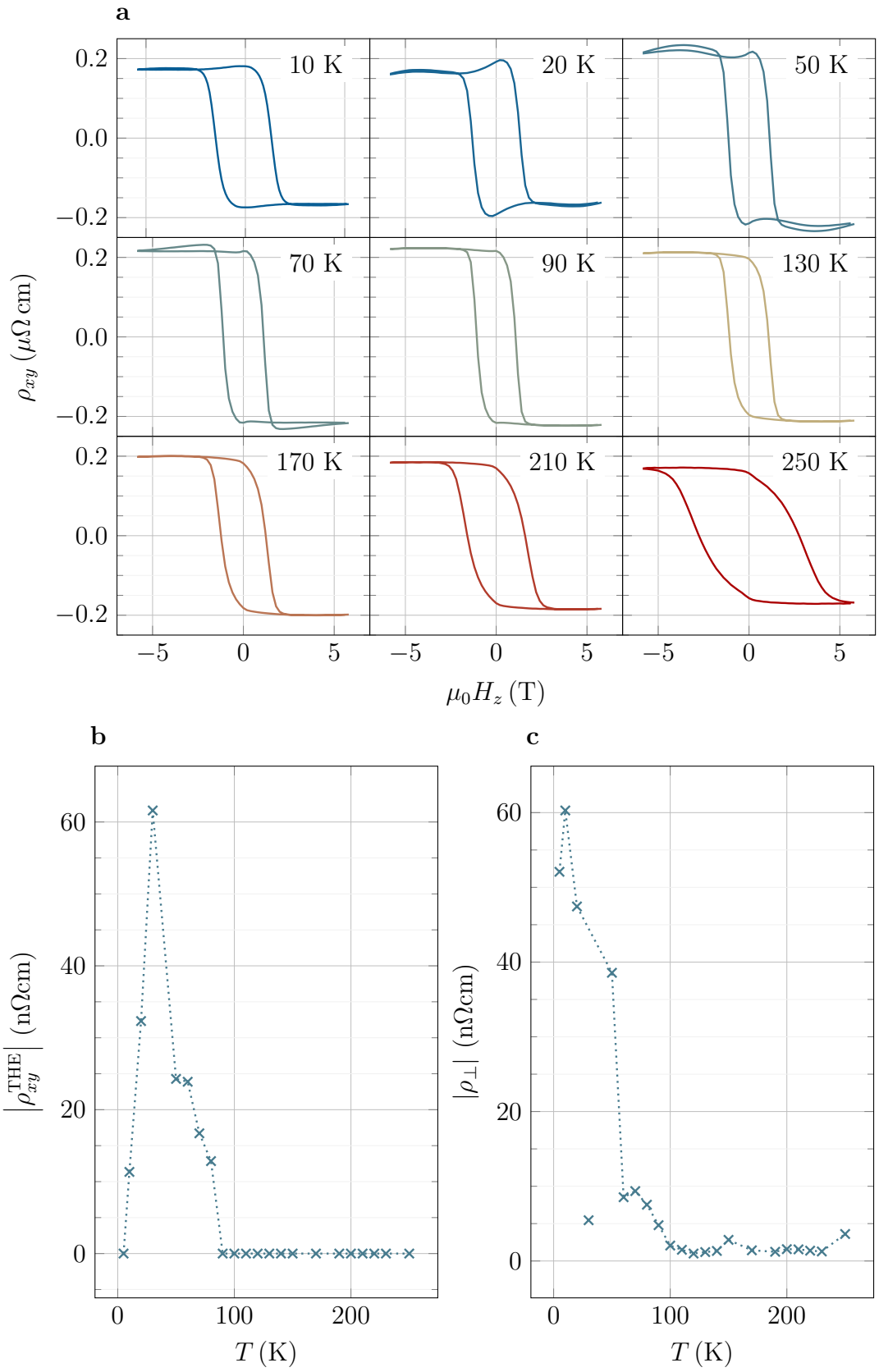

Figure 2.11: Field dependence of transverse resistivity ρ_{xy}. **a** Transverse resistivity during a field sweep for multiple temperatures. **b** Temperature dependence of the ρ_{xy}^{THE} magnitude. **c** Temperature dependence of the $\rho_\perp$ magnitude.

of the coercive field temperature dependence, see [60]). This demonstrates that the hysteresis is present both in the collinear and in the noncollinear antiferromagnetic phases of Mn_5Si_3. Note that the magnitude of the loops remains approximately unchanged in the whole studied temperature region ($\approx 0.2\,\mu\Omega$cm), even when approaching the Néel temperature.

The Néel temperature, where the phase transition from the collinear phase to paramagnetic occurs, is supposed to lie above 210 K. This transition seems to be gradual [60]. At 250 K, we cannot reach the saturation field and thus we detect only a minor loop. The hysteresis completely disappears at higher temperatures above 250 K [60].

In the collinear antiferromagnetic phase below 210 K, the presence of a hysteresis loop implies that Mn_5Si_3 evinces an unusual time-reversal symmetry breaking mechanism. Untill recently, such breaking was reported only for noncollinear antiferromagnets [48] (see Sec. 2.1.1). This $\mathcal{T}$-symmetry-breaking phenomenon can be identified with the predicted anomalous (spontaneous) Hall effect, which we already confirmed in Mn_5Si_3 [24, 60]. The collinear ordering should persist up to approx. 80 K, and in this region (80–210 K), the hysteresis loop has a standard rectangular shape with no THE contribution. This is quantitatively illustrated in Fig. 2.11b. In this temperature region, the magnitude of ρ_{xy}^{THE} is virtually zero.

Zero THE contribution indicates vanishing spin chirality and probable collinear ordering of the material. This observation is of particular importance, because the collinearity of the Mn_5Si_3 high-temperature AFM phase has not been directly confirmed so far. The existence of cAFM phase in a thin-film Mn_5Si_3 is only based on theoretical models and neutron scattering experiments on bulk Mn_5Si_3.

When the temperature is decreased below 80 K to the noncollinear magnetic phase, the shape of the hysteresis loops starts to change (see Fig. 2.11a), and a "bump" in the vicinity of the zero field starts to form. This is presumably a manifestation of the topological Hall effect [24]. The THE contribution is present only in the low-temperature phase, as visible from its temperature dependence in Fig. 2.11b. Interestingly, it peaks around 30 K and then drops to zero if the temperature is further decreased to 5 K. The finite topological Hall contribution confirms that the magnetic moments have nontrivial spatial configuration and Mn_5Si_3 entered its noncollinear antiferromagnetic phase.

Another possible manifestation of the topological Hall effect may be observed in the hysteresis loops measured at 70 K and 50 K. The loop does not close at high fields, and the signal is not entirely saturated. However, this observation remains to be fully understood.

We illustrated that the THE contribution can be used to indicate the changing magnetic order. Interestingly, the overall trend of the $|\rho_{xy}^{\mathrm{THE}}|$ temperature dependence is also followed by $|\rho_\perp|$ as illustrated in Fig. 2.11c: The $|\rho_\perp|$ signal is substantial below 60 K and drops to zero above 90 K. This correlation may indicate that the origin of the $\rho_\perp$ signal is also connected to the noncollinear spin structure of the noncollinear phase. However, the origin of $\rho_\perp$ has yet to be fully comprehended.

2.3.2 Thermoelectric transport

The thermoelectric study of the Mn_5Si_3 magnetic properties was conducted analogically to the electronic transport by sweeping the external magnetic field along the z-axis. The magnitude of the external field was again changed between ±6 T with a ramping rate of 0.5 T/min. The in-plane thermal gradient was created by using the external macroscopic heaters.

The field-sweep signals were measured using various values of power applied to the resistive heater: they ranged from 0.25 W to 2.1 W. The base temperature of the chip carrier was set and maintained below 70 K. The substantial heating power not only generated an in-plane temperature gradient but was also significantly warming up the whole sample: the temperature of the sample was substantially different compared to the chip carrier. The actual temperature on the sample was determined from the measurement of resistivity on Mn_5Si_3 contacts and by comparing it against the known temperature dependence of ρ_{xx} (see Sec. 2.2.3). Using this method, we managed to determine the sample temperature with the precision of ±2 K. However, such precision is not enough to evaluate the temperature gradient, which is in the order of units of K/mm. The temperature calibration was more precise at higher temperatures, from which we estimate that the temperature gradient ranged from 0.1 to 2 K/mm.

If we were able to determine the temperature gradient with sufficient precision, we could then calculate longitudinal and transverse Nernst signal S_{xx} and S_{xy} using the following definition (compare it with Eq. (2.5)):

$$S_{xx} = \frac{V_{xx}/l_{xx}}{|\nabla T|}, \quad S_{xy} = \frac{V_{xy}/l_{xy}}{|\nabla T|}, \tag{2.15}$$

where l_{xx} and l_{xy} is length of the longitudinal and transverse contact, $|\nabla T|$ is the magnitude of the temperature gradient [63]. However, we shall present the measured data only in arbitrary (normalized) units due to the lack of precise measurement of $|\nabla T|$.

In Fig. 2.12 we show an example of the transverse thermovoltage signal as measured. Since the direction of the temperature gradient was not as well defined as the current direction in a conventional magnetotransport experiment, we measured a mix of longitudinal and transverse resistance contributions to the V_{xx} and V_{xy} signals. Therefore, symmetrization and antisymmetrization with respect to H_z was used as an essential tool for the separation of the longitudinal and transverse contributions to the particular V_{xx} and V_{xy} signals. Also, in order to remove the contribution of the ordinary Nernst effect from the measured data, we subtracted a linear slope from the S_{xy} signal.

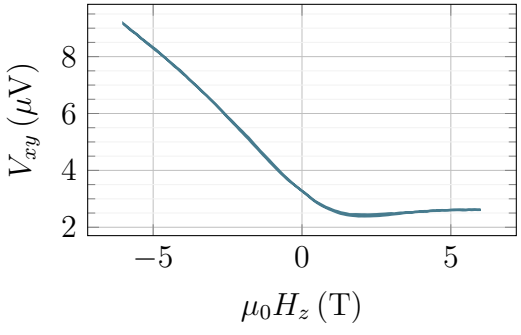

Figure 2.12: An example of raw V_{xy} thermoelectric data as measured at 25 K using 1.29 W of heating power, resulting in the sample temperature of 128 K and a rough estimate of the temperature gradient 0.5 K/mm.

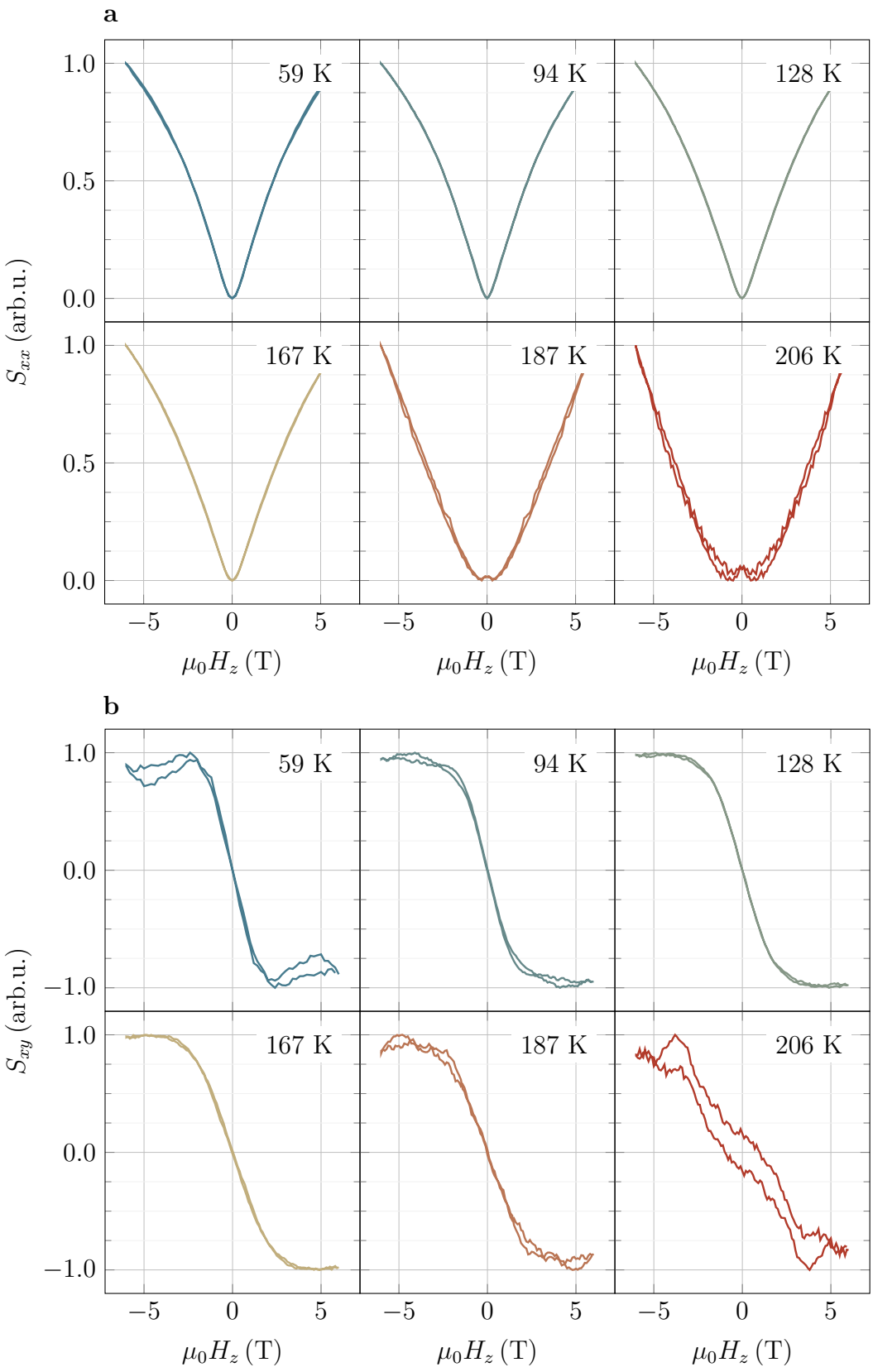

Figure 2.13: **a** Longitudinal and **b** transverse thermoelectric signal S_{xx} and S_{xy} as a function of the external magnetic field H_z, applied in the out-of-plane direction, for multiple temperatures. The sample temperature was determined by a calibration of Mn_5Si_3 contacts resistivity.

The dependence of the S_{xx} and S_{xy} signals on the applied field H_z is shown in Fig. 2.13 for different sample temperatures, which were determined by the above-described calibration procedure. Let us now analyze the longitudinal (symmetrized) and transverse (antisymmetrized) signals separately.

Longitudinal signal The longitudinal signal presented in Fig. 2.13a displays a pronounced thermal magnetoresistance with its characteristic behaviour. Due to the uncertainty in the temperature gradient, we cannot compare the magnitude of the signals for different temperatures. However, there is also an apparent qualitative change in the shape of the curves with temperature: At low temperatures, the magnetoresistance curve is convex, while above 170 K, the dependence starts to show concave behaviour. This feature can be explained as a consequence of mixing of two (or more) contributions to S_{xx} with different temperature dependencies. Possible candidates for these two components would be thermal OMR and thermal AMR, in analogy with the similar signals observed in the electronic transport. Note that unlike in ρ_{xx} in Fig. 2.8, there is no sign change in S_{xx} around 160 K; however, the change of the S_{xx} character (convex/concave) occurs at a very similar temperature as the sign change of ρ_{xx}.

Transverse signal The transverse signal in Fig. 2.13b shows a clear saturation for temperatures up to 190 K. Above 200 K, the noise level is too high to extract reliable curves. In addition, we observe an artefact in the form of an effective loop opening related to temperature drift removal. Although there is a pronounced saturation in the S_{xy} signal, we did not see any hysteretical behaviour. This is in striking contrast with the ρ_{xy} signal, where a strong hysteretic loop opening was observed.

For clarity, a comparison between ρ_{xy} and S_{xy} is shown in Fig. 2.14 for three selected temperatures (note that all the signals are normalized to saturated values). Except for the lack of hysteresis, there is also a difference in the saturation field: The saturation occurs at higher fields in the thermoelectric experiment, with the shift of approximately 1.5 T. This feature holds mainly in the collinear phase at

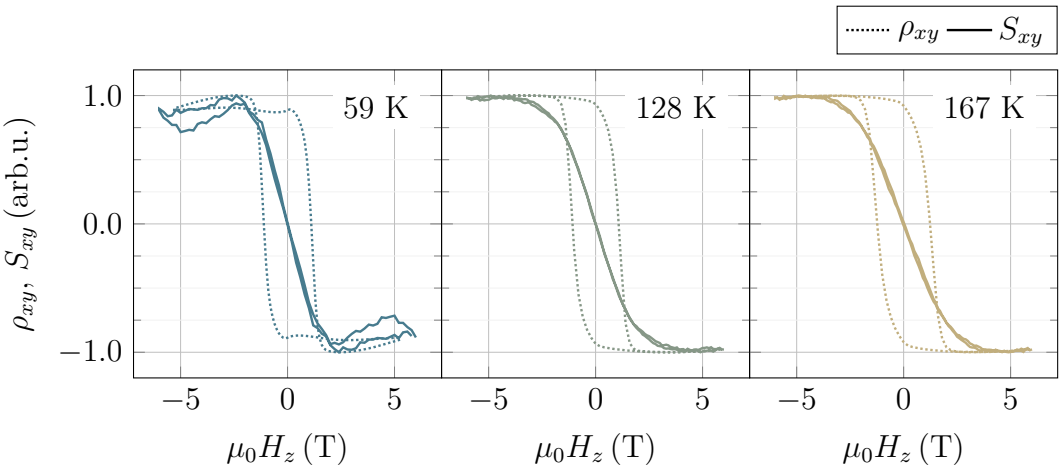

Figure 2.14: Comparison of transverse signal in an electric and thermoelectric field sweep ρ_{xy} and S_{xy} for three different temperatures (we chose ρ_{xy} curves measured at similar temperatures, i.e. 60 K for 59 K, 130 K for 128 K, and 170 K for 167 K).

128 K and 167 K. Note also that at 59 K a broadening appears at high fields. A similar broadening is also present in the ρ_{xy} curve at high fields, which suggests a magnetic origin of this feature.

The seeming mutual inconsistency between the hysteresis loop measured in thermoelectric and electronic transport could be understood in terms of breaking in small domains. Indeed, the transverse contact on which we collect S_{xy} is substantially longer than a width of a Hall bar for the ρ_{xy} measurement (compare w_a and l_b in Fig. 2.4 — l_b is 76× larger). However, this explanation is not in agreement with our test experiment, where we measured ρ_{xy} on devices with a substantially different width of the Hall bar (by the factor of 40×). The hysteresis did not disappear, and the coercive field was exactly the same. Therefore, we may conclude that domain formation is not a valid mechanism of the change in the hysteresis loop shape. The second possible explanation is that the hysteresis may disappear because of the large heating powers and the not very well defined temperature gradient direction. This mechanism could be confirmed by a simultaneous measurement of S_{xy} and ρ_{xy} on the same device. Such experiment is currently planned by our collaborating group at the University of Konstanz.

Chapter 3

Magnetooptical study of Mn_5Si_3

Magnetooptical measurements are a standard probe of materials with magnetic order. Magnetooptical effects (such as the magnetooptical Kerr or Faraday effects) are widely used in characterization and technical applications, and advanced techniques such as the time-resolved magnetooptical spectroscopy are valuable tools for investigating processes related to spin dynamics.

Though widely used on ferromagnets and even antiferromagnetic systems [64, 65], no magnetooptical study has been performed in any altermagnetic material so far. Mn_5Si_3 is a promising candidate for such a study as it shows a strong spontaneous Hall effect, a transport counterpart of the magnetooptical Kerr effect.

This chapter introduces magnetooptical phenomena and their relation to the magnetotransport effects. Then we describe optical and magnetooptical methods. Finally, we present the results of our experiments which probe the static magnetooptical response of Mn_5Si_3.

3.1 Theoretical introduction

In 1845, Michael Faraday observed that the polarization plane of linearly polarized light rotates when the beam passes through glass with an external magnetic field applied parallel to the direction of propagation [64]. This phenomenon — the Faraday effect — is a notorious example of a magnetooptical effect. Magnetooptics (MO) deals with the interaction of light and matter when an external or, in a more general view, also internal magnetic field is present. In the following, we shall focus on the phenomenological description of magnetooptical phenomena relevant to this thesis. Then we discuss the relationship between magnetooptical and magnetotransport phenomena. Finally, we will give a brief overview of antiferromagnets known to show a magnetooptical response.

3.1.1 Phenomenological description of magnetooptical effects

From the theoretical point of view, it is convenient to study magnetooptical phenomena in two distinct geometrical configurations depending on the relative orientation of a light wave vector $\boldsymbol{k}$ and a magnetic field $\boldsymbol{H}$: When the light travels along the magnetic field ($\boldsymbol{k} \parallel \boldsymbol{H}$), we talk about the *Faraday geometry*, whereas for $\boldsymbol{k} \perp \boldsymbol{H}$, the term *Voigt geometry* is used [64].

The magnetooptical response can be observed either when the light is transmitted through a MO active medium, or when it is reflected. Although the latter situation is more relevant for this thesis, we will first describe the magnetooptical response in the simpler transmission geometry.

When light passes through a magnetic medium, there exist two light eigenmodes which are conserved [11]. In the Faraday geometry, these modes correspond to the left- and right-handed circular-polarized modes σ^+ and σ^-. In contrast, the eigenmodes in the Voigt geometry are two linearly polarized waves $\sigma^\parallel$ and $\sigma^\perp$ that are parallel and perpendicular to the magnetic field [11]. Magnetooptical phenomena then arise because the complex index of refraction differs for the two eigenmodes in each of the geometries.

In general, birefringence can be explained as a consequence of the difference in a real part of the refraction indices for the two orthogonal polarization eigenmodes. Similarly, dichroism (polarization-dependent absorption) stems from the difference in imaginary part of refractive indices. Combining these phenomena with the different complex refractive indices for the eigenmodes in both the Faraday geometry (complex refractive indices $\tilde{n}^+$ and $\tilde{n}^-$) and the Voigt geometry (complex refractive indices $\tilde{n}^\parallel$ and $\tilde{n}^\perp$), we arrive at four magnetooptical effects that act on the incident linearly polarized beam as follows:

- the *magnetic circular birefringence* in the Faraday geometry caused by $\Re\left(\tilde{n}^+\right) \neq \Re\left(\tilde{n}^-\right)$ induces rotation of the polarization plane,
- the *magnetic circular dichroism* in the Faraday geometry caused by $\Im\left(\tilde{n}^+\right) \neq \Im\left(\tilde{n}^-\right)$ induces polarization ellipticity,
- the *magnetic linear birefringence* in the Voigt geometry caused by $\Re\left(\tilde{n}^\parallel\right) \neq \Re\left(\tilde{n}^\perp\right)$ induces polarization ellipticity,
- the *magnetic linear dichroism* in the Voigt geometry caused by $\Im\left(\tilde{n}^\parallel\right) \neq \Im\left(\tilde{n}^\perp\right)$ induces rotation of the polarization plane [64].

Analogical effects can occur when linearly polarized light reflects from a magnetic medium. However, rotation and ellipticity cannot be directly linked to dichroism or birefringence of the eigenmodes, as the relevant quantity is now the Fresnel coefficients of reflection $\tilde{r}$ for the eigenmodes.

If we consider the normal incidence geometry, the Fresnel reflection coefficient is $\tilde{r} = (1 - \tilde{n})/(1 + \tilde{n})$, assuming the material is placed in vacuum with $\tilde{n} = 1$. In the Faraday geometry ($\boldsymbol{k} \parallel \boldsymbol{H}$), the linearly polarized light then gains ellipticity if the absolute values $|\tilde{r}^+|$ and $|\tilde{r}^-|$ differ. The plane of polarization is rotated, if $\arg\left(\tilde{r}^+\right) \neq \arg\left(\tilde{r}^-\right)$. Similarly for the Voigt geometry, the rotation is induced by $|\tilde{r}^\parallel| \neq |\tilde{r}^\perp|$ and the ellipticity arises when $\arg\left(\tilde{r}^\parallel\right) \neq \arg\left(\tilde{r}^\perp\right)$ [11].

The above-described relations are general. Now, we will focus on a specific case of materials with an internal magnetic field characterized by magnetization $\boldsymbol{M}$. The first magnetooptical effect, in which magnetization points out of the sample plane and the light incidence is normal ($\boldsymbol{M} \parallel \boldsymbol{k} \parallel \boldsymbol{n}$ with the sample surface normal $\boldsymbol{n}$), is known as the *polar magnetooptical Kerr effect* (PMOKE). The second configuration with $\boldsymbol{M} \perp \boldsymbol{k} \parallel \boldsymbol{n}$ is known as the *Voigt effect in reflection* (VER). These effects are illustrated in Fig. 3.1. Since both PMOKE and VER

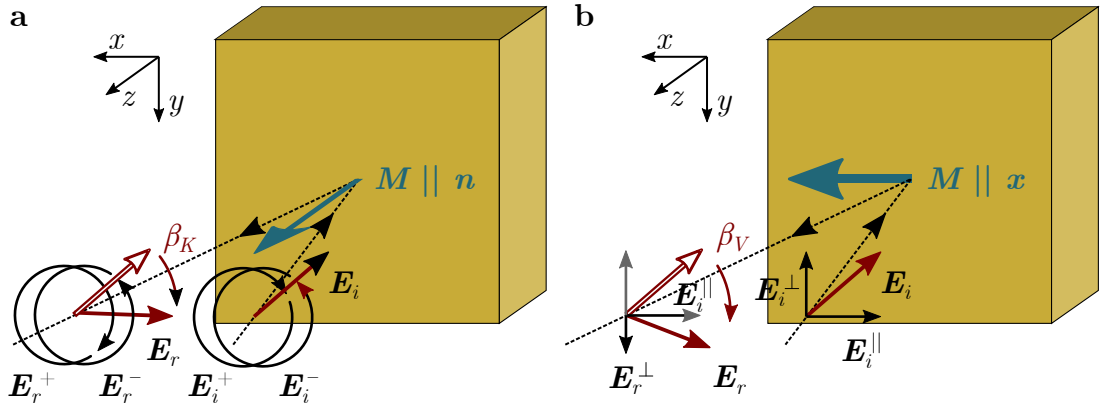

Figure 3.1: Magnetooptical effects in reflection in the near-normal incidence geometry. **a** Rotation of the polarization plane due to the polar Kerr effect arises from a phase shift between left- and right-handed circular-polarized light. **b** Different absolute values of reflective coefficients for linearly polarized light along the magnetization vector and perpendicular to it induce rotation of the polarization plane in the Voigt effect in reflection. Adapted from [11].

are crucial for the further analysis of our experimental results, we shall introduce them in more detail.

The magnetooptical response can be quantified by solving the electromagnetic wave equation for electric intensity $\boldsymbol{E}$:

$$\nabla\left(\nabla\cdot\boldsymbol{E}\right)-\nabla^2\boldsymbol{E}=-\mu\hat{\varepsilon}\ddot{\boldsymbol{E}}+\mu\hat{\sigma}\dot{\boldsymbol{E}}, \tag{3.1}$$

where $\hat{\varepsilon}=\hat{\varepsilon}(\omega)$ and $\hat{\sigma}=\hat{\sigma}(\omega)$ are the permittivity and conductivity tensors, respectively [66]. Assuming the solution is a plane wave $\boldsymbol{E}(\boldsymbol{r},t)=\boldsymbol{E}_0e^{-i(\omega t-\boldsymbol{k}\cdot\boldsymbol{r})}$, the equation can be rewritten as:

$$k^2\boldsymbol{E}_0-\boldsymbol{k}\left(\boldsymbol{k}\cdot\boldsymbol{E}_0\right)-\omega^2\mu_0\hat{\varepsilon}_{\text{eff}}\boldsymbol{E}_0=0 \tag{3.2}$$

where we introduced $\hat{\varepsilon}_{\text{eff}}=\hat{\varepsilon}_0+i\hat{\sigma}_{\text{eff}}/\omega$. The structure of the effective permittivity tensor $\hat{\varepsilon}_{\text{eff}}$ is governed by the tensor $\hat{\sigma}_{\text{eff}}$ that characterizes the response of the whole system (both the electrons and the lattice) to the perturbing electric field [66]. The magnetooptical response of PMOKE and VER can be derived by inserting a problem-specific form of $\hat{\varepsilon}_{\text{eff}}$ to Eq. (3.2), which gives the refractive indices of the corresponding eigenmodes.

Polar Kerr effect When a cubic crystal shows magnetization, the originally isotropic permittivity tensor gains non-diagonal elements. For magnetization $\boldsymbol{M}$ pointing along the z-axis and the polar Kerr effect configuration $\boldsymbol{M}\parallel\boldsymbol{k}\parallel\boldsymbol{n}$ (see Fig. 3.1a), the effective permittivity tensor is following [66]:

$$\hat{\varepsilon}_{\text{eff}}=\varepsilon_0\begin{pmatrix}\epsilon_{xx} & \epsilon_{xy} & 0\\ -\epsilon_{xy} & \epsilon_{xx} & 0\\ 0 & 0 & \epsilon_{zz}\end{pmatrix}, \tag{3.3}$$

with dimensionless components ϵ_{ij}. Solving Eq. (3.2) leads to the eigenmodes of the left- and right-handed circular-polarized waves and to an expression for their complex refractive indices [66]:

$$\tilde{n}_{\pm}^2 = \epsilon_{xx} \pm i\epsilon_{xy}. \tag{3.4}$$

From $\tilde{n}^{\pm}$ and the corresponding reflective coefficients $\tilde{r}^{\pm}$, one can obtain an expression for the reflected electric intensity and thus calculate [11] the angle of polarization plane rotation β_K for a linearly-polarized incident wave as follows:

$$\beta_K = \Re\left(\frac{\epsilon_{xy}}{\sqrt{\epsilon_{xx}}\,(1-\epsilon_{xx})}\right). \tag{3.5}$$

Note that in Eq. (3.5), we suppose that the polarization changes are small, i.e. $|\epsilon_{xy}| \ll |\epsilon_{xx}|$ [11].

Voigt effect in reflection In contrast to PKE, in the Voigt effect we assume the magnetization to lie in the sample plane. We shall suppose that it points along the x-axis. In this configuration and again assuming a cubic symmetry of the crystal, the effective permittivity tensor becomes [11]:

$$\varepsilon_{\text{eff}} = \varepsilon_0 \begin{pmatrix} \epsilon_{xx} & 0 & 0 \\ 0 & \epsilon_{yy} & \epsilon_{yz} & 0 \\ 0 & -\epsilon_{yz} & \epsilon_{zz} & 0 \end{pmatrix}. \tag{3.6}$$

Similarly to PMOKE, solving Eq. (3.2) leads to linearly-polarized eigenmodes with the polarization plane parallel or perpendicular to the magnetization direction, and with the corresponding refractive indices $\tilde{n}^{\parallel}$ and $\tilde{n}^{\perp}$ [11]:

$$\tilde{n}_{\perp}^2 = \epsilon_{xx}, \tag{3.7}$$

$$\tilde{n}_{\parallel}^2 = \epsilon_{yy}\left(1 + \frac{\epsilon_{yz}^2}{\epsilon_{yy}^2}\right). \tag{3.8}$$

Under the assumption of small polarization changes, the angle of polarization plane rotation β_V can be expressed as [11]:

$$\beta_V \approx \frac{n_0 \,\sin 2\theta_i}{2(n_0^2-1)}\left(\epsilon_{xx} - \epsilon_{yy} - \frac{\epsilon_{yz}^2}{\epsilon_{yy}}\right), \tag{3.9}$$

where θ_i is the angle between the polarization plane of the incident beam and magnetization; n_0 is the isotropic refractive index (in the absence of magnetization).

In general, phenomenological description of the electromagnetic interaction in crystals with magnetic order is based on the knowledge of the appropriate material tensors. For the above-described response of PMOKE and VER, we chose the permittivity tensor; however, one could also use conductivity or permeability tensors since the symmetry of these tensors is the same for given crystal class [67]. If we now focus only on the ferromagnetic ordering defined by the magnetization

vector $\boldsymbol{M}$, and we further suppose that the permittivity dependence on $\boldsymbol{M}$ is weak, the cartesian components of the permittivity tensor can be expanded as follows [67]:

$$\varepsilon_{ij} = \varepsilon_{ij}^{(0)} + K_{ijk}M_k + G_{ijkl}M_kM_l + \ldots, \tag{3.10}$$

where $\varepsilon_{ij}^{(0)} = \varepsilon_{ji}^{(0)}$ are the components of the permittivity tensor for $\boldsymbol{M} = 0$. K_{ijk} are components of the linear magnetooptic tensor, while G_{ijkl} represents the quadratic magnetooptic tensor [67].

From the Onsager relations (see Eq. (2.3) for comparison), it follows that [67]:

$$\varepsilon_{ij}(\boldsymbol{M}) = \varepsilon_{ji}(-\boldsymbol{M}). \tag{3.11}$$

The diagonal components of the effective permittivity tensor obey the relation $\epsilon_{ii}(\boldsymbol{M}) = \epsilon_{ii}(-\boldsymbol{M})$ and are thus an even function of the magnetization. Furthermore for the off-diagonal elements, it can be proved [67] that $\epsilon_{ij}(-\boldsymbol{M}) = -\epsilon_{ij}(\boldsymbol{M})$ in cubic crystals, and so they are an odd function of magnetization. Surprisingly, the same holds also for hexagonal crystals with the D_{6h} point group (e.g. Mn_5Si_3 [68]). These observations have interesting consequence for the Kerr and Voigt rotation angles β_K and β_V in Eqs. (3.5) and (3.9): As ϵ_{xy} is an odd function of magnetization and ϵ_{xx}, ϵ_{yy}, and ϵ_{yz}^2 are even, the angle β_K is odd in magnetization, while β_V is even.

It is important to note that we demonstrated the parity of the Kerr and Voigt angles with respect to the magnetization vector explicitly for a cubic crystal. However, it is generally assumed that the polarization rotation induced by the PMOKE is an odd function of magnetization while the VER rotation is even [66].

3.1.2 Relationship between magnetooptical and transport phenomena

As stated above, electromagnetic processes in a crystalline solid can be described by different tensors: either by permittivity, conductivity, or permeability. From the phenomenological point of view, the relationship between conductivity $\hat{\sigma}$ and permittivity $\hat{\varepsilon}$ tensors is established by the standard formula [69]:

$$\hat{\varepsilon}(\omega) = \hat{\varepsilon}_0 + \frac{i\hat{\sigma}(\omega)}{\omega}, \tag{3.12}$$

where ω is a frequency of the electromagnetic radiation. The tensor $\hat{\sigma} = \hat{\sigma}(\omega)$ is understood as the *optical* conductivity tensor as it is usually used in the context of optical frequencies.

The natural question is how the optical conductivity relates to the electronic transport conductivity $\tilde{\sigma} \neq \tilde{\sigma}(\omega)$, defined by Ohm's law $\boldsymbol{j} = \tilde{\sigma}\,\boldsymbol{E}$. In the context of the magnetooptical phenomena, $\tilde{\sigma}$ is usually considered to correspond to the zero-frequency limit of $\hat{\sigma}$ as $\tilde{\sigma} = \hat{\sigma}(\omega \to 0)$ [66, 69–73].

The connection between $\hat{\varepsilon}(\omega)$ and $\hat{\sigma}(\omega)$ ($\tilde{\sigma}$ respectively), provides a method to link directly the magnetooptical and magnetotransport effects. For example, the expression for the Kerr rotation angle (see Eq.(3.5)) can be written using the carthesian components of the optical conductivity tensor as follows [73]:

$$\beta_K = \Re\left(\frac{-\sigma_{xy}}{\sigma_{xx}\sqrt{1 + i\sigma_{xx}/\omega}}\right), \tag{3.13}$$

which is directly proportional to the off-diagonal component σ_{xy} of the $\hat{\sigma}$ tensor. This links the PMOKE to the anomalous Hall effect which arises from the non-zero $\tilde{\sigma}_{xy}$. The AHE is thus often considered as a zero-frequency limit of the Kerr effect, with which it shares also the same symmetry with respect to magnetization [66, 70–72, 74, 75]. Similarly, the Voigt effect in reflection can be viewed as a finite-frequency counterpart of transverse anisotropic magnetoresistance [66].

In recent years, there have been attempts to go beyond the phenomenological description and try to link the magnetooptical and magnetotransport effects by their microscopic origin, i.e., band exchange-splitting and spin-orbit coupling [73, 75]. Multiple works investigated the zero-frequency limit of PMOKE together with the anomalous Hall effect both from experimental and theoretical points of view [69, 71–74]. For example, Kim et al. compared [72] the low-frequency limit of PMOKE with AHE for the ferromagnetic $SrRuO_2$, and concluded that the corresponding conductivities agree for the energy above 200 meV. In a low energy regime below 200 meV the difference is a result of intraband transitions and also a significant contribution of the extrinsic anomalous Hall effect to the magnetotransport signals. The relation between PMOKE and AHE was also studied by the first-principles Berry curvature calculations for ferromagnetic $SrRuO_2$ [72], or antiferromagnetic Mn_3Sn [71].

From the purely experimental point of view, Balk et al. demonstrated [74] differences in the PMOKE and AHE signal in the noncollinear antiferromagnet Mn_3Sn. They observed pronounced hysteresis loops when measuring both the PMOKE and AHE responses as a function of the external magnetic field [74]. However, the coercive field of both signals was substantially different, and a drop in the observed signals due to a magnetic-phase transition occurred at a lower temperature for the AHE (by 10 K). This indicates that the relationship between PMOKE and AHE is not entirely straightforward. Magnetooptics probes rather the magnetic properties of the sample surface compared to the electronic transport that is entirely driven by the bulk properties of the material[74].

In this section, we extensively used magnetization as the magnetic-ordering vector, which is zero for antiferromagnets. In the following, we shall discuss that the Kerr and Voigt magnetooptical response may also be present in magnetically ordered materials with zero net magnetization, as shown recently in several works, including Balk et al. [74].

3.1.3 Magnetooptics and antiferromagnets

A spontaneous magnetooptical response can be present also in ordered materials with zero net magnetization — antiferromagnets. The Voigt effect and other magnetooptical phenomena with an even dependence on effective magnetization can be, in principle, present in any antiferromagnet [65]. The Voigt effect was confirmed in multiple collinear antiferromagnets such as CuMnAs [65], or $GdVO_4$ [76], and for most of the AFM systems, it provides the only optical tool for studying their magnetic ordering.

Until recently, it was supposed that fully compensated antiferromagnets could not show any magnetooptical signal that would be odd in effective magnetization as the contributions from the oppositely oriented magnetic sublattices would

cancel out [65]. This certainly holds for most of the well-known collinear AFM systems where the MOKE or any other type of linear MO effect is absent. However, several theoretical and experimental studies show the Kerr response is possible in antiferromagnets with a noncollinear spin structure: In 2015, Feng et al. predicted [70] the presence of MOKE response in a class of noncollinear antiferromagnets Mn_3X with X being Rh, Ir, and Pt as a consequence of the strong spin–orbit coupling and the breaking of double band degeneracy. The predicted signals were comparable to transition-metal magnets (e.g. bcc iron). A strong PMOKE signal was measured later in another manganese-based noncollinear antiferromagnet Mn_3Sn at room temperature [71, 74].

On the other hand, altermagnets — such as Mn_5Si_3 — display large spontaneous Hall response as well as anisotropic magnetoresistance (see Chapter 2). Based on the analogy of the magnetooptical and transport effects described in the previous section, it is reasonable to assume that in Mn_5Si_3, also PMOKE and VER may be present. In the following, we focus on the experimental detection of these effects.

3.2 Samples and magnetooptical methods

In this section, we shall briefly describe two different samples of Mn_5Si_3 we used for the optical measurements, and then we introduce the experimental methods. These include the measurement of spectral reflectance and a variety of the magnetooptical experiments.

3.2.1 Samples

We chose the same thin layers of Mn_5Si_3 that revealed strong AHE in our previous studies [60]. Two different samples were studied, both grown using molecular-beam epitaxy on an intrinsic Si (111) substrate. The first sample, denoted as `MnSi80` consisted of 25 nm of Mn_5Si_3, whereas the second one labelled as `MnSi82` had a Mn_5Si_3 layer of 23 nm. Similarly to the sample `MnSi163` used for the transport experiments in this thesis, these samples also contained a small MnSi contribution which is ferromagnetic below 30 K [77]: `MnSi80` contained 9 % of MnSi, while in the second sample `MnSi82` it was only 4 %. Both of these samples were already thoroughly studied using magnetotransport [60], and they show strong spontaneous Hall conductivity. The sample growth and the structural and magnetic characterization were done by our collaborating group at the Interdisciplinary Center of Nanoscience of Marseille. The samples remained unpatterned for the optical experiments.

As a reference for the MO measurements, we used intrinsic silicon (100) wafer.

3.2.2 Measurement of spectral reflectance

Essential information about the band structure can be obtained by the spectrum of reflected light. For this purpose, we measure the spectral dependence of the sample reflectance. Reflectance is defined as the ratio of the radiant flux reflected by the surface and the radiant flux received by the surface. A schematic of the experimental setup is shown in Fig. 3.2: The light source was a xenon wide-spectral-range lamp, and the light was focused on a sample in an optical,

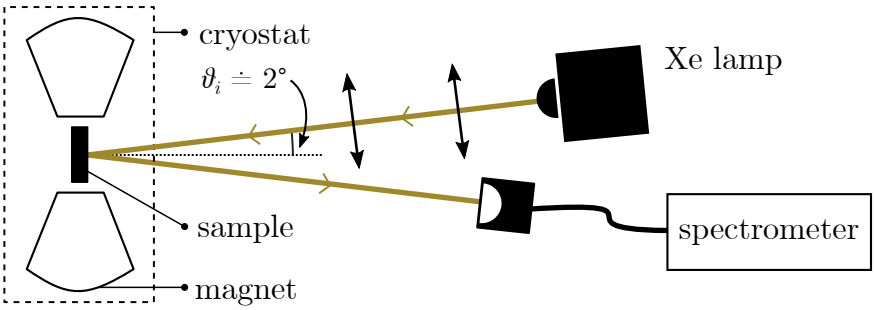

Figure 3.2: Schematic of a spectral reflectance measurement. The light source was a xenon lamp.

closed-cycle, and low-vibration cryostat (*Montana Instruments*). The cryostat enabled measurements in the temperature region of 4–350 K, and an in-plane magnetic field of up to 900 mT was generated using an integrated electromagnet. The beam was in near-normal incidence, with an incidence angle $\vartheta_i \approx 2°$. The reflected light was then collected by an optical fibre and spectrally analyzed by a grating spectrometer (*Andor Solis*) with a spectral range of 250–1000 nm.

In order to calculate reflectance, a calibration of the setup was required. The light emitted by the Xe lamp is spectrally inhomogeneous, also optical components in the setup have different transmittance for different wavelengths. Therefore we cannot directly use the raw signal from the spectrometer (counts per wavelength). For the calibration, we measured a raw reflected light spectrum from an intrinsic Si (100) wafer. The spectrum was compared with reflectance R calculated from the known values of real and imaginary refractive index n and κ of silicon [79] using a standard formula:

$$R = \frac{(n-1)^2 + \kappa^2}{(n+1)^2 + \kappa^2}. \qquad (3.14)$$

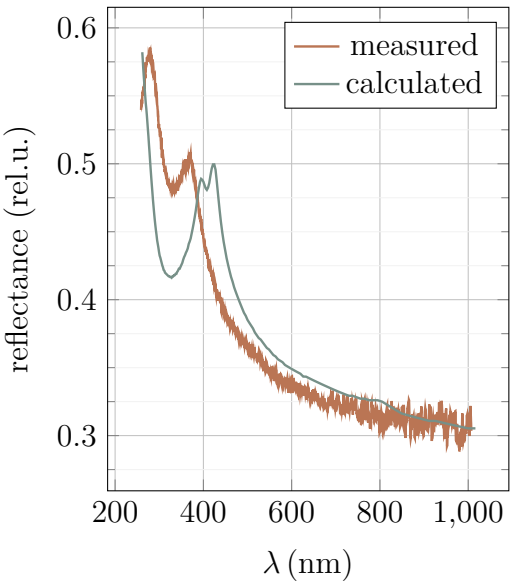

Figure 3.3: Spectral reflectance for a GaAs wafer as calculated from refractive indices [78] and measured using calibration on Si (100).

By dividing the measured and the calculated spectral dependence of R, we got a calibration factor for each wavelength by which the measured data have to be multiplied to obtain real reflectance (in relative units). In order to verify the accuracy of this calibration, we did a control measurement on a GaAs wafer which also has a well-known spectral dependence of reflectance [78]. Both the measured and the calculated reflectance of GaAs are shown in Fig. 3.3. Though there is a good correspondence both in shape and in magnitude of the spectrum, the measured dependence is spectrally shifted to shorter wavelengths. Furthermore, the dependence below 400 nm is

also qualitatively different. This procedure reveals a limitation of the calibration process, which must be considered when analyzing the data.

3.2.3 Magnetooptical measurements

The main part of the optical experiments was dedicated to magnetooptics. We used three different experimental setups for the magnetooptical study of Mn_5Si_3. The first experimental setup was optimized to measure the temperature dependence of the magnetooptical response during a *temperature sweep*. In this experiment, the temperature was continuously varied at a constant rate. The other two setups were designed for the measurement of *field sweeps*, i.e. the experiment where the magnetooptical response is measured as a function of the external magnetic field magnitude: The field was applied either perpendicularly to the sample surface, which we shall call *polar field geometry* or in the sample plane in the *longitudinal field geometry*.

The *temperature sweep* experiments were performed in the Magnetooptical laboratory of the Department of Chemical Physics and Optics at Charles University, while the magnetooptical *field sweeps* were carried out in the laboratory of Magnetooptics Research Prague (MORP) at the Institute of Physics of Charles University. Let us now describe the particular experiments in more detail.

Temperature sweeps A schematic of our experimental setup for temperature sweeps is in Fig. 3.4a: The light source was a supercontinuum pulse laser (*SuperK Extreme*) with a tunable filter (*SuperK Varia*) which has a spectral range from 480 nm to 840 nm with a tunable bandwidth. The laser power was always set to 1 mW with a spot size of roughly 100 μm. The sample was placed in a chamber of a closed-cycle cryostat (*ARS cryogenics*) with a temperature range of 20–300 K. The chamber was inserted between the poles of a two-dimensional vector electromagnet with the field orientation in the plane xy, generating a maximum field of 207 mT.

The linearly-polarized laser beam was focused on the sample under a small angle of incidence of 1°. We detected a change in the plane of polarization of the reflected beam by an optical bridge. The bridge consists of a polarizer (`P` in Fig. 3.4a) that splits the incident beam into its s-polarized and p-polarized components. The intensity of these two components were detected using semiconductor photodetectors `A` and `B`, as in Fig. 3.4a. Both signals were processed by differential pre-amplifiers that generated their sum V_+ and difference V_-. These two signals were then measured by the lock-in detection method for which the light intensity was modulated by a mechanical chopper (`Ch` in Fig. 3.4a) and analyzed by two lock-in amplifiers *Stanford Research Systems SR830* [80].

The rotation of the plane of linearly polarized light by the angle β_{MO} can be calculated from the sum and the difference signals V_+ and V_- as:

$$\beta_{MO} = \frac{V_-}{2 \cdot A\, V_+}, \tag{3.15}$$

where A as the ratio of V_- and V_+ amplification [81]. This expression holds for small angular deviations where $\beta_{MO} \approx \sin(\beta_{MO})$. Also, the resulting β_{MO} is only a relative change with respect to the initial stage (defined i.e. by temperature or magnetic field magnitude).

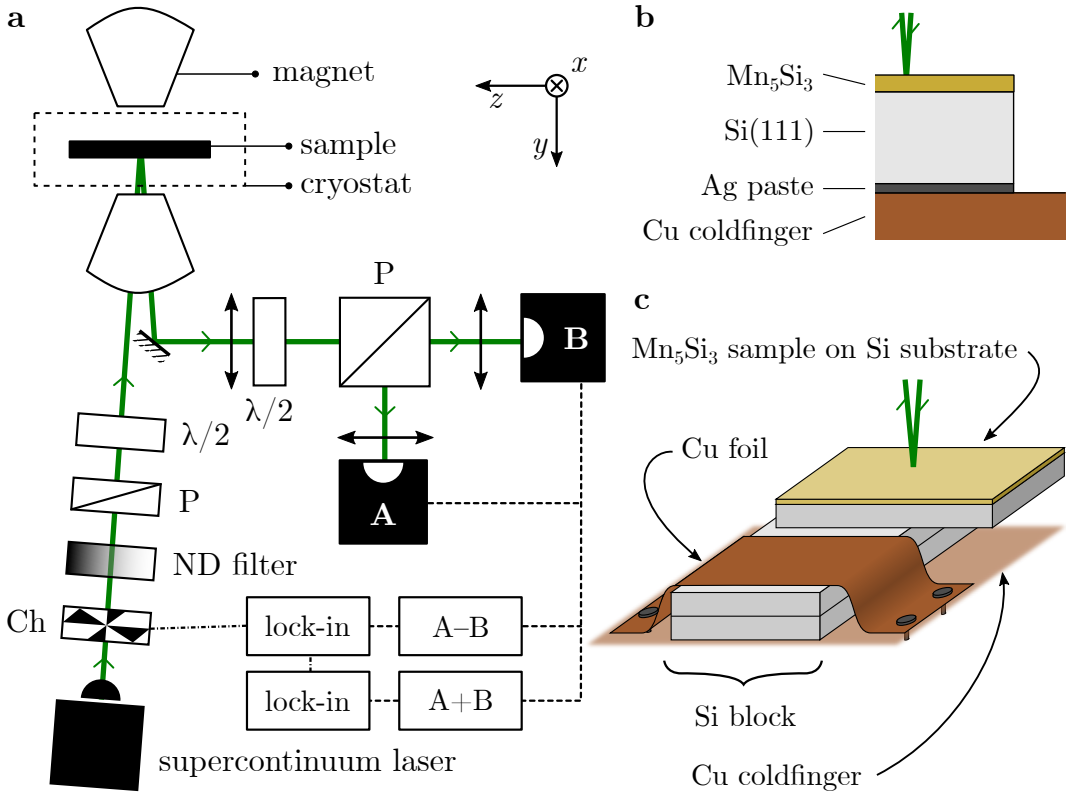

Figure 3.4: Schematic of a temperature-sweep experiment. **a** Schematic of the experimental setup where `P` is a polarizer, $\lambda/2$ is a half-wave plate, and `A`, `B` are photodetectors. **b** A "strained" configuration where the sample is strained due to the different coefficients of thermal expansion of silicon and copper. **c.** A "strainless" configuration where the thermally induced strain is relaxed through the multiple layers of a silicon substrate.

The measurement was done for multiple orientations of linear polarization of the incident light to identify the particular magnetooptical effect responsible for the signal. The polarization plane of the incident laser beam is determined by the angle θ, which is zero for the linear polarization along the x-axis and 90° for the polarization along the z-axis. See Fig. 3.4a for the coordinate system.

During the experiments, we encountered several issues related to strain effects induced by temperature. Therefore, we employed two different approaches to attach the sample to a copper holder (*coldfinger*) in the cryostat. In the first method (see Fig. 3.4b), the sample is simply glued directly to the coldfinger using a silver paste. Here, however, the different coefficients of thermal expansion of copper ($15.2 \cdot 10^{-6}\,\mathrm{K}^{-1}$ at 300 K [82]) and the silicon substrate ($1.4 \cdot 10^{-6}\,\mathrm{K}^{-1}$ at 200 K [82]) lead to a substantial mechanical strain during a temperature sweep where the temperature can change by more than 200 K. Therefore we introduced a different, strain-free configuration illustrated in Fig. 3.4c where the thermally-induced strain is suppressed. The sample is supported by two 0.5 mm Si layers through which the strain relaxes. To improve the heat transfer between the sample and the cold finger, a copper foil was glued to the top side of the silicon block and connected with the coldfinger (see Fig 3.4c).

Field sweeps in polar field geometry An analogical experimental setup to the previous section was used for the polar field sweeps. Here, the magnetic field is applied perpendicular to the sample plane as shown in Fig. 3.5: To obtain a spectral resolution, we used two different laser-diode systems for 405 nm (*Matchbox SLM*) and 785 nm (*Newport LDM*) with 1 mW of laser power. The sample was placed in a closed-cycle cryostat with an incorporated electromagnet (*Montana Instruments*). The available temperature range was 4 K to 350 K, and the maximum magnetic field was 900 mT. In this configuration, the laser beam was directed through a hole in one of the pole pieces. As for the temperature sweeps, we used an optical bridge for the measurement of a change of the linear polarization angle together with a lock-in detection method and *SR830* lock-in amplifiers. The polarization angle θ of the incident beam has the same convention, i.e. θ is zero for the linear polarization along the x-axis and 90° for the polarization along the z-axis.

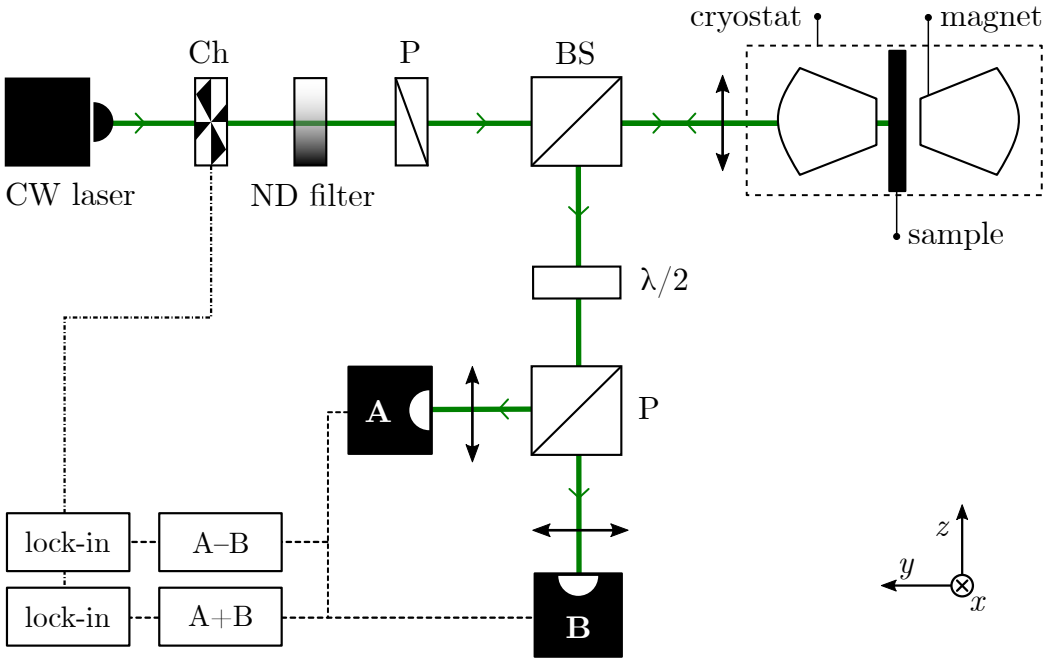

Figure 3.5: Schematic of the experimental setup, designed for measurement of the field sweep in the perpendicular magnetic field. Here `P` is a polarizer, $\lambda/2$ is a half-wave plate, `A`, `B` are photodetectors, and `A+B`, `A−B` are differential preamplifiers.

In order to test the response of the setup itself to the applied magnetic field (i.e. Faraday effect in windows and lenses, mechanical motion), we measured the rotation of the polarization plane as a function of H_z on a nonmagnetic silicon substrate and in our Mn_5Si_3 sample at room temperature. As the Néel temperature for Mn_5Si_3 is below 250 K, the sample should be paramagnetic at room temperature and show no magnetooptical response. However, even in the paramagnetic phase of Mn_5Si_3 and in pure silicon, we measured nontrivial field-dependent signals as shown in Fig. 3.6. Fig. 3.6a shows a polarization dependence of the measured field-sweep signal at 785 nm. In contrast, Fig. 3.6b captures field sweeps for two different wavelengths and for a fixed polarization of $\theta = 45°$. Clearly, the signal is substantially stronger at 405 nm and is polarization-dependent. We measured virtually identical dependencies also for the silicon

substrate. This leads us to a conclusion that a substantial signal artefact (the signals are up to 1 mrad for 405 nm) originates in the experimental setup itself. As the magnetic field outside the cryostat was negligible (as confirmed also by a Gauss-meter), we suspected the cryostat windows had a nontrivial magnetooptical response. This assumption was confirmed when we removed the windows for a room-temperature experiment, which resulted in suppression of the artefact signal. A measurement at low temperatures required the windows to be installed, and thus we could not remove the artefact entirely. However, we managed to suppress it using the optimal configuration, i.e., the wavelength of 785 nm and 45° polarization, which is apparent from Fig. 3.6. For the polar geometry, this posed no limitation for our experiment since the polar Kerr effect, observed in this experiment, is polarization independent.

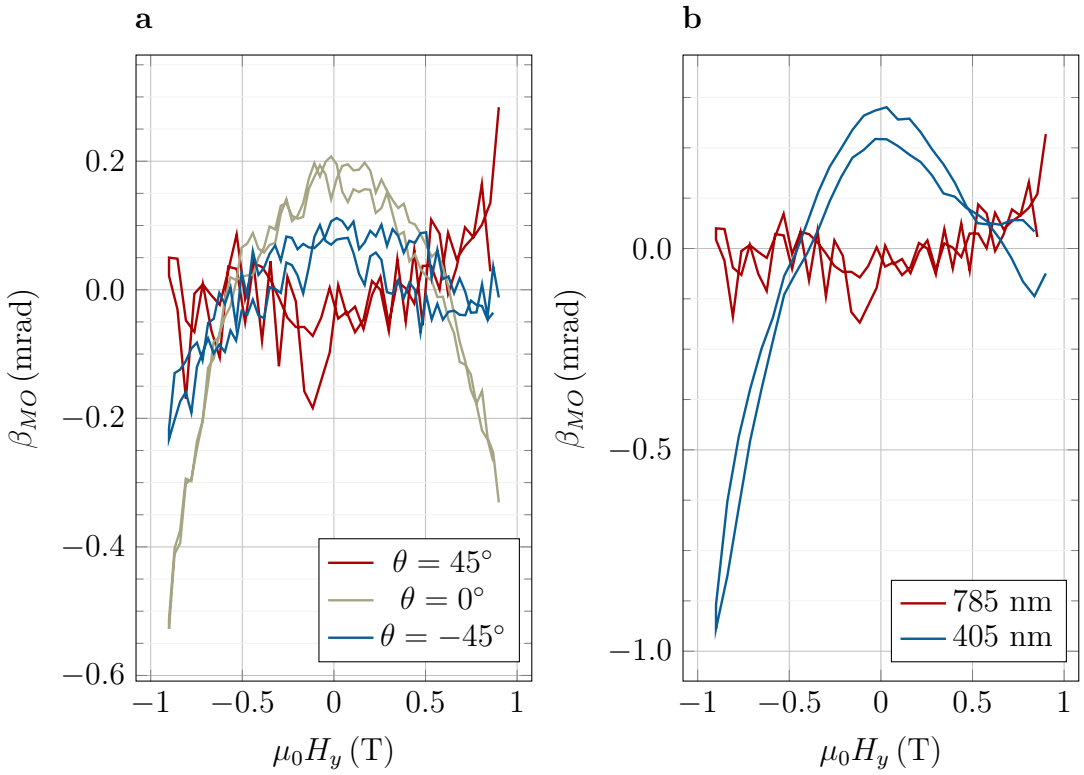

Figure 3.6: A field sweep of a magnetooptical artefact originating in the cryostat windows as measured on a Mn_5Si_3 sample at 296 K. **a** The dependence for multiple orientations of linear polarization at 785 nm. **b** A field-sweep for different wavelengths and $\theta = 45°$.

Field sweeps in longitudinal field geometry The experimental setup for field sweeps in longitudinal geometry was analogous to the previous magnetooptical methods and is shown in Fig. 3.7. Here, the light source was again a laser diode system with either 405 nm or 785 nm wavelength and power set to 1 mW. Since this geometry is suitable for observation of the quadratic MO effects that are strongly polarization-dependent, a polarizer and a half-wave plate defined the polarization orientation. The sample was placed in a closed-cycle cryostat (*Montana Instruments*) so that the magnetic field vector was lying both in the sample plane and in the plane of incidence. The measurement was done in the reflection geometry with the angle of

incidence of approximately 2°. We measured the change in the linear polarization by an optical bridge and a lock-in method as described above.

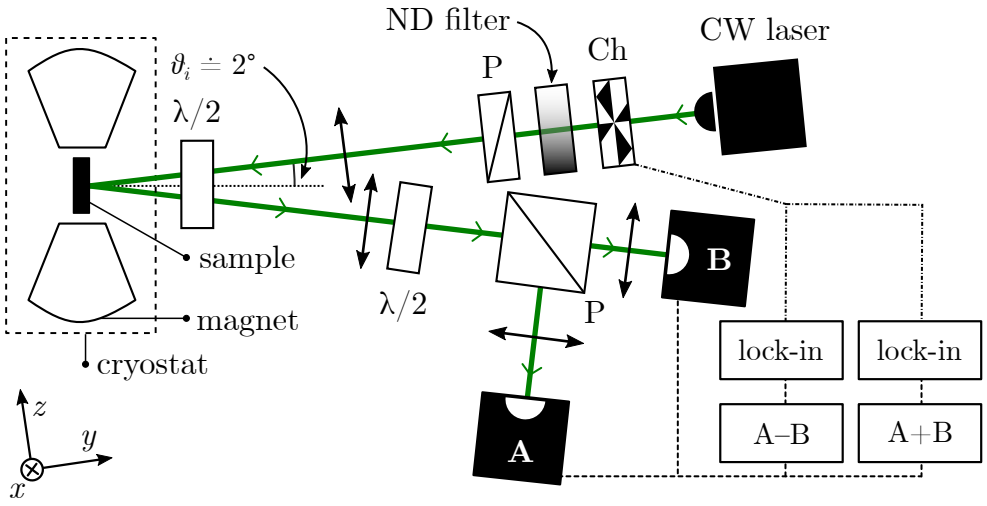

Figure 3.7: Experimental setup for detection of the magnetooptical signals with a longitudinal geometry of the magnetic field. Here `P` is a polarizer, $\lambda/2$ is a half-wave plate, `A`, `B` are photodetectors, and `A+B`, `A−B` are differential preamplifiers. The angle of incidence was approximately 2°.

Similarly to the polar field sweeps, there was an artefact originating in the cryostat window, however substantially weaker. It was not strongly polarization- or wavelength-dependent, and we managed to suppress it within the data processing.

3.3 Experimental results

In this chapter, we present results of the magnetooptical study of a band-split collinear antiferromagnet (altermagnet) Mn_5Si_3. Therefore, this survey aims to highlight the perspective magnetooptical experiments that could complement the already successful transport methods described above. A magnetooptical study of the altermagnets is particularly important because of the perspective of studying their domain structure by magnetooptical microscopy or the in-situ measurement of their magnetic properties on spintronic devices.

We show the results of both the different magnetooptical methods as well the basic optical characterization of Mn_5Si_3 by optical spectroscopy. The aim is to understand the optical behaviour of the material, as well as to identify the dominant MO effect that could be used for potential MO magnetometry.

3.3.1 Spectral reflectance

Measurement of spectral reflectance was done in order to identify particular transitions in the band structure that could be related to the magnetic ordering of the material. For this purpose, we measured a temperature dependence of the reflectance spectrum in the sample `MnSi80` as shown in Fig. 3.8a. The spectra were processed using the Si (100) calibration as described above. As an additional reference experiment, we performed an ellipsometric measurement using

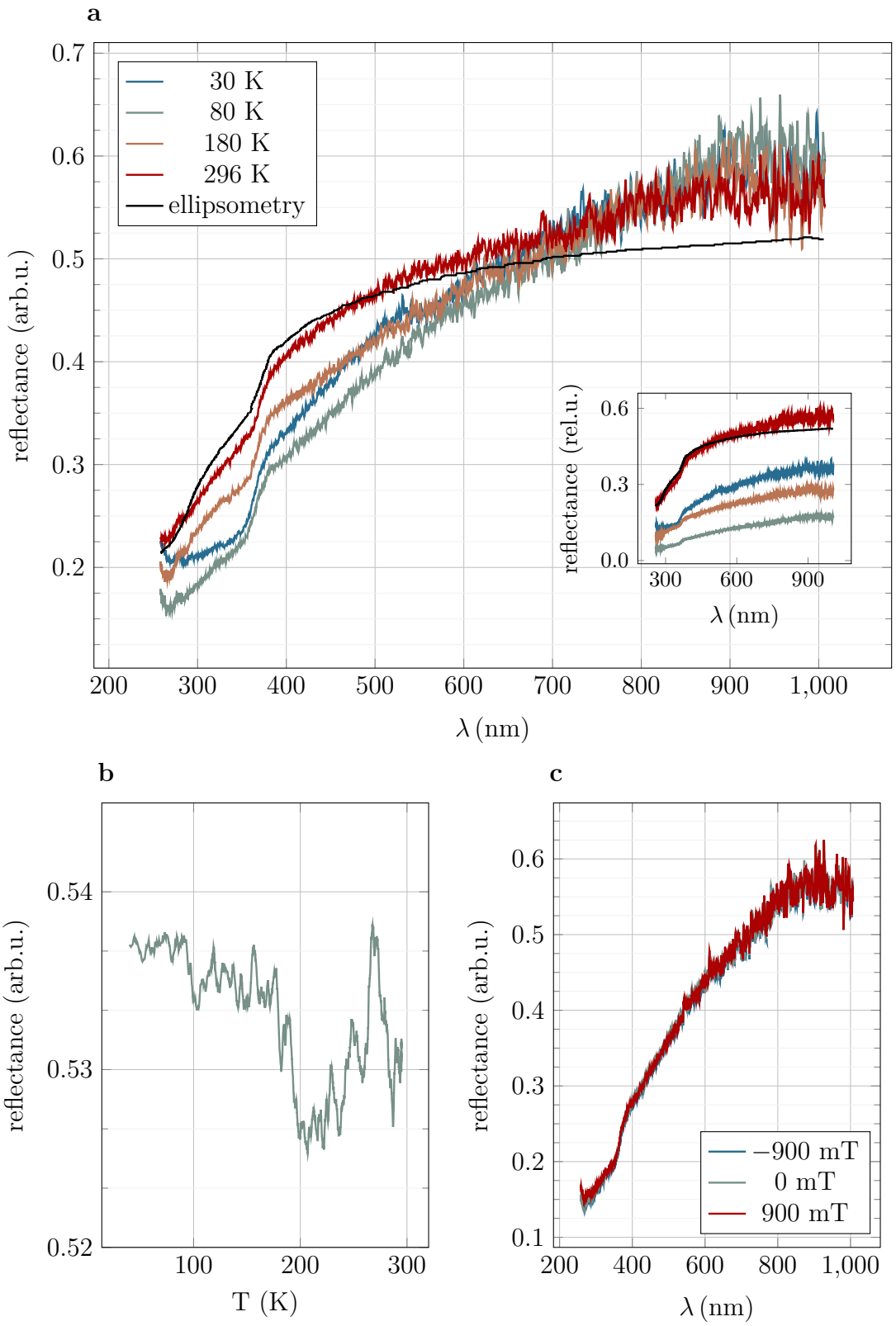

Figure 3.8: Reflectance spectra of `MnSi80`. **a** Spectral reflectance measured at four different temperatures. The inset shows raw calculated curves. The data in the main panel were normalized with respect to the signal at room temperature. The normalization is based on the reflectance at 785 nm. Both graphs include a spectrum measured by an ellipsometer. **b** The temperature dependence of reflectance measured for a fixed wavelength of 785 nm. **c** Spectral reflectance measured at 180 K for three magnitudes of an magnetic field applied in the sample plane.

a spectroscopic ellipsometer (*Woollam RC2*). The data are included in Fig. 3.8a for comparison.

The agreement between the measurement using an ellipsometer and our configuration with a spectrometer is both quantitatively and qualitatively good. The only discrepancy occurs for longer wavelengths above roughly 800 nm where the spectra start to differ by approximately 10 %. As the agreement for the short wavelengths is relatively good, we suppose that the calibration discussed above performs well for the Mn_5Si_3 sample at room temperature.

The same experiment was performed at low temperatures, where we observed a substantial decrease in reflectance as visible in the raw data in the inset of Fig. 3.8a. From our measurement of reflectance temperature dependence (see Fig. 3.8b), we know that the reflectance at 785 nm is weakly temperature-dependent and varies by less than 4 % between 293 K and 30 K. Therefore, we suppose that the change of the absolute reflectance in the inset of Fig. 3.8a is an experimental artefact, supposedly caused by mechanical movement of the sample in the cryostat during the cooldown process. It is most likely not an intrinsic property of Mn_5Si_3. We thus scaled the low-temperature data to the room temperature dependence using the reflectance at 785 nm, which is shown in the main graph of Fig. 3.8a (ellipsometry measurement is unchanged). The same scaling was also done in Figs. 3.8b,c.

To investigate the response of the band structure to an external magnetic field, we also measured the reflectance spectra with an in-plane magnetic field of $\pm$900 mT as shown in Fig. 3.8c.

The reflectance spectrum in Fig. 3.8a does not show any specific feature which would systematically change with temperature. Apart from the general trend of increasing reflectance with wavelength, we find one characteristic feature in the spectrum — the reflectance step around 360 nm. Another Mn-based noncollinear antiferromagnet Mn_3NiN evinces a peak in reflectance around 400 nm [83] supposedly connected with an optical transition to the $3d$ states of the magnetic manganese atoms [84]. This opens up the possibility that the observed step in Mn_5Si_3 may also be connected with these transitions. Furthermore, it motivates us to focus on the near UV region within our magnetooptical experiments. However, to make any definite conclusions about the observed spectrum, it would be necessary to compare it with an *ab initio* calculation.

For our further magnetooptical measurements, it was particularly interesting to study the influence of an external magnetic field on the band structure. If there was any change with the magnetic field present, it would enable us to select interesting spectral regions for further measurements. However, as apparent from Fig. 3.8c, the external magnetic field does not influence the spectrum at all. We suppose that the field of 900 mT is not strong enough to manipulate the magnetic moments of Mn_5Si_3.

3.3.2 Magnetooptical measurements

The magnetooptical measurements were performed as an optical analogy to our transport experiments in Chapter 2. We conducted two types of magnetooptical experiments: The aim of *temperature sweeps* was to pinpoint the phase transition temperatures where magnetooptical signals are expected to change. The second

method — *field sweeps*, served as a direct counterpart to the transport measurements of the anomalous Hall effect and anisotropic magnetoresistance, with the perspective of evaluating the magnitude of the corresponding magnetooptical phenomena, i.e. the polar Kerr effect and the Voigt effect.

Temperature sweeps During a temperature sweep, we measured the magnetooptical response β_{MO} as a function of the sample base temperature set in the cryostat. The temperature was gradually changed between 305 K and 30 K with a constant rate of $8\,\mathrm{K\,min^{-1}}$. The measurement was done for different wavelengths, linear polarizations of the incident light, and magnitudes of the applied out-of-plane magnetic field (with the magnitude of 207 mT). Results of the temperature sweeps, measured in the sample `MnSi80` are shown in Fig. 3.9 for the wavelength of 600 nm, 0° polarization, and no external magnetic field applied. Besides the magnetooptical signal β_{MO} in Fig. 3.9a, we also present the normalized reflectance signal (corresponds to normalized V_+) in Fig. 3.9b.

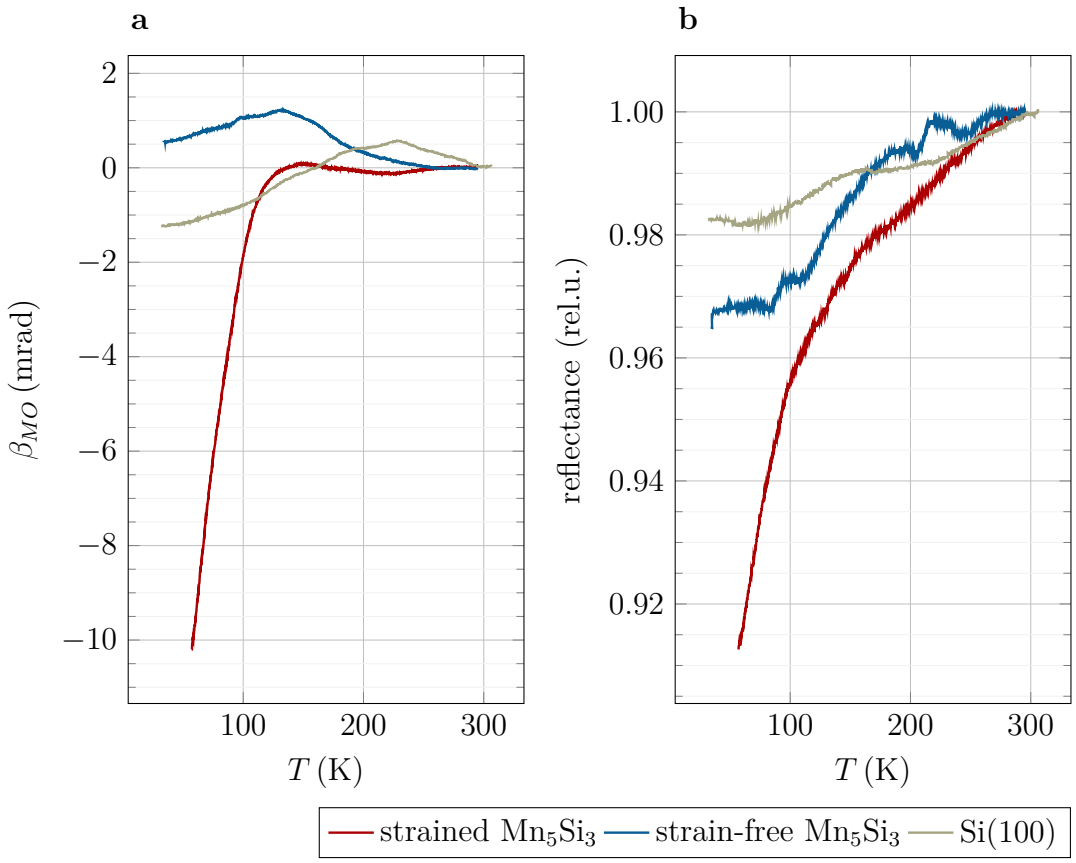

Figure 3.9: Temperature sweep measured on `MnSi80` using the wavelength of 600 nm and no magnetic field. The "strained" curve was measured using a configuration in Fig. 3.4b, whereas the strain-free experiment is based on a technique described in Fig. 3.4c. A control measurement on Si(100) is also included. **a** Temperature dependence of the magnetooptical signal. **b** Temperature dependence of normalized reflectance.

Firstly, we performed the measurement with the sample `MnSi80` directly glued on the coldfinger, as drawn in Fig. 3.4b. This temperature sweep is shown in Fig. 3.9 and is labelled as "strained". Then we attached the sample on additional Si substrates, in a configuration drawn in Fig. 3.4c. The corresponding measurement

is labelled as "strain-free" in Fig. 3.9. Finally, the same experiment was repeated on a silicon substrate used as a nonmagnetic reference (silicon was directly glued to the coldfinger). We measured both the temperature sweeps down (from room temperature to 30 K) and then up. The signal always regained its initial value (i.e. 0 mrad since the optical bridge was balanced at the beginning of the measurement). This means that the curves in Fig. 3.9 are not a result of a (e.g., mechanical) drift in time, but they correspond to a real optical signal.

By comparing the data in Fig. 3.9a, it is apparent that the "strained" configuration shows a strong MO response below 120 K. At higher temperatures, the signal drops rapidly to zero. The largest change occurs between 100 K and 50 K. In contrast, the "strain-free" measurement yields a signal comparable with the nonmagnetic silicon response. This leads us to the conclusion that the large magnetooptical signal in the "strained" configuration is induced by the mechanical stress of the sample, caused by the different coefficients of thermal expansion for silicon and copper. This strain should be relaxed in the "strain-free" configuration through multiple silicon layers. This conclusion is supported by observing structural changes on the sample surface when removing the sample from the coldfinger after the first measurement. A microscopic image (taken using an optical microscope with magnification 20×) of the damaged sample is shown in Fig. 3.10. Note that a plain, undamaged layer has no structure. This could result from the Mn_5Si_3 layer being torn by the quickly relaxed strain after removing the sample.

Furthermore, there might be an additional explanation for the large β_{MO} signal related to the structural changes of the sample. The reflectance of the strained sample changes by approx. 9 % (see Fig. 3.9b) in the whole temperature region, which indicates that the strain induces changes in the crystal structure in Mn_5Si_3. The structural changes may result in the changed optical properties, i.e. reflectance and optical anisotropy, which can be observed both in reflectance and in β_{MO} (Fig. 3.9a,b).

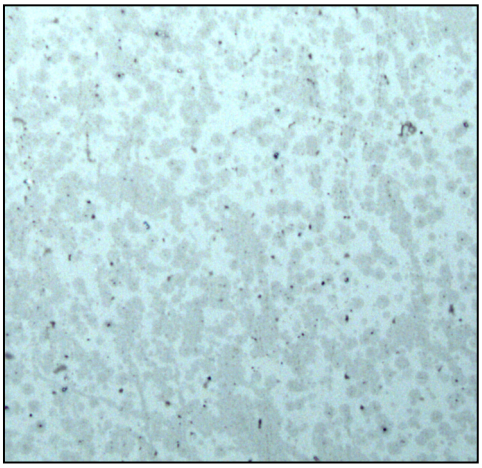

Figure 3.10: A optical microscope image of a damaged sample `MnSi80` after multiple temperature cycles. Magnified 20×.

During the measurement in the "strain-free" configuration, we experienced issues with the reproducibility of the data. Therefore in Fig. 3.9, we present only those dependencies which we were able to replicate. For example, we do not present the temperature sweeps with an external magnetic field applied, which was unreproducible. The β_{MO} signal observed in Mn_5Si_3 during a "strain-free" measurement could be a sign of an intrinsic magnetooptical response of Mn_5Si_3, or it may be connected with the thermally induced strain in the cryostat windows. The latter explanation could also hold for the measurement of the nonmagnetic silicon substrate. However, the

signal on silicon can also be connected with strain-induced optical anisotropy as the silicon layer was directly glued to the coldfinger.

Finally, we shall discuss a possible effect of the strain on the spin structure of Mn_5Si_3. The substantial magnetooptical signal in the "strained" measurement is present only at low temperatures (see Fig. 3.9a), which could indicate that only the low-temperature noncollinear phase of Mn_5Si_3 is sensitive to strain. The phase transition from collinear to noncollinear phase occurs below 100 K (the precise phase-transition temperature is sample-dependent), matching the observed increase of the signal. However, an alternative explanation can be given that the strain generates purely optical anisotropy in the sample. This effect may not be linear and appears only when a particular strain threshold is exceeded. The nature of our results prevents us from making any definitive conclusions about the origin of the effect, and further studies are required. Particularly, we suggest measuring the effect of strain by using piezo stressors rather than the not well-defined thermal strain.

Despite all the debatable points, we are positive to claim that Mn_5Si_3 shows a robust optical response when exposed to mechanical strain. The signals may be connected with nonmagnetic optical anisotropy, or they result from strain-induced magnetooptics. The latter possibility justifies our further study of Mn_5Si_3 by magnetooptical magnetometry, i.e. field sweeps.

Sweeps in polar field geometry Transport measurements of Mn_5Si_3 show a strong spontaneous Hall response [60]. Here, we aim to explore the magnetooptical analogy of the AHE — the polar Kerr effect.

For the polar field sweeps, we applied an external magnetic field perpendicular to the sample surface and measured the magnetooptical response β_{MO} in reflection with the near-normal incidence of the light. The magnetic field was swept between $\pm$900 mT, and the rotation of polarization plane β_{MO} was detected at various temperatures, covering both antiferromagnetic phases of Mn_5Si_3. We used different orientations of linear polarization and two wavelengths of incident light — 405 nm and 785 nm, to suppress the experimental artefacts (see Sec. 3.2.3) and to maximize the magnetooptical response.

An example of the measured data is shown in Fig. 3.11 for the sample `MnSi82`. Here, we present the field sweeps at four temperatures: 60 K in the noncollinear phase, 180 K in the collinear phase, and the transition temperature between these antiferromagnetic phases (90 K). The last temperature, 210 K, is at the transition to the paramagnetic state. The curves were measured using the laser wavelength of 785 nm with two different orientations of polarization. As there was also a nontrivial field-dependent signal at room temperature (see Fig. 3.6), which supposedly originated in the cryostat windows — and thus does not significantly change with temperature — we subtracted this data from the curves measured at lower temperatures.

The geometry of our setup for polar field sweeps corresponds to the measurement scheme of the polar Kerr effect. When measuring the field dependence of the magnetooptical signal, the PMOKE would manifest as a saturating hysteresis loop [74]. However, we do not observe any systematic field-dependent signal in these data. The reason might be a relatively high noise level, with a peak-to-peak noise amplitude of approximately 0.2 mrad. The dominant noise source was presumably

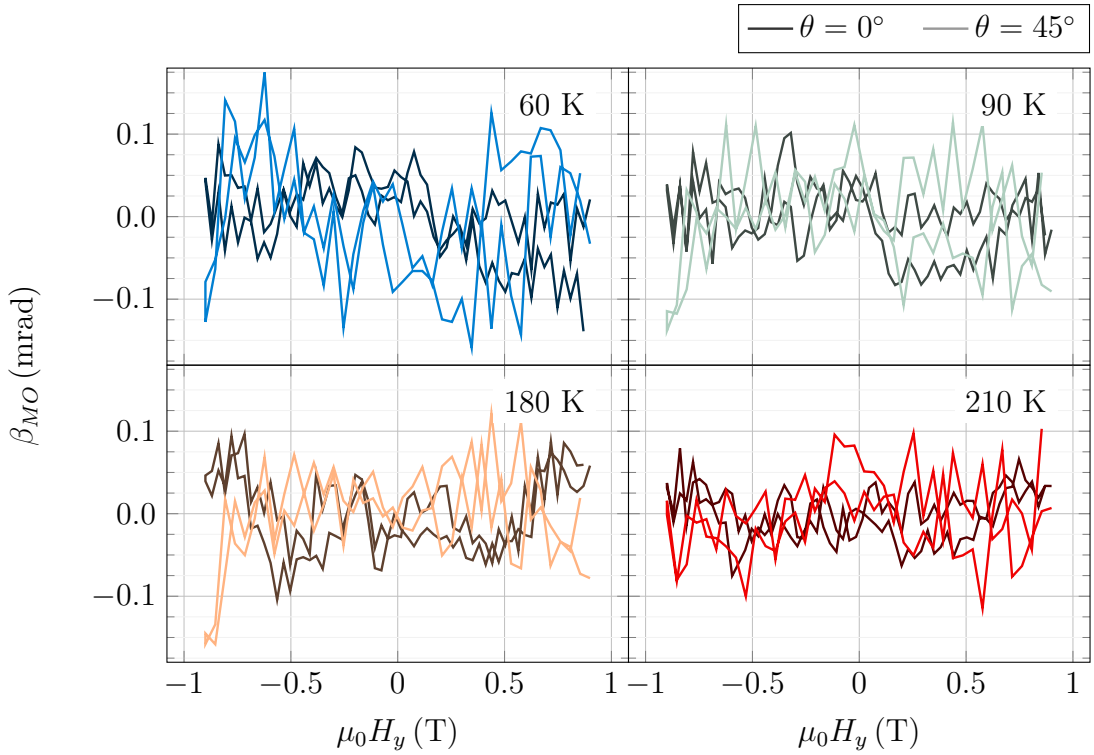

Figure 3.11: Dependence of magnetooptical response β_{MO} on the applied magnetic field during a polar field sweep for the sample `MnSi80`. The measurement was done for multiple temperatures and two orientations of polarization: $\theta = 0°$ is shown in dark and $\theta = 45°$ in light color.

a cone-shaped pole piece of the electromagnet, through which the light entered the cryostat chamber. The aperture in the piece was of comparable size to the beam width resulting in the beam being partially cut.

We can thus conclude that any Kerr response, if present, is beyond the resolution of our experimental setup, which is about 200 μrad. This is not surprising, as the Kerr response of an example noncollinear bulk antiferromagnet Mn_3Sn is only about 350 μrad for the fully saturated hysteresis loop [71]. With the field of 900 mT, we are not even close to saturation [60] and the possible formation of domains would diminish the magnetooptical signal even more.

We also cannot exclude that Mn_5Si_3 does not show any spontaneous Kerr response at all. Magnetooptical phenomena in Mn_5Si_3 have not yet been theoretically predicted, and we entirely rely on the analogy between the MO and transport effects (see Sec. 3.1.2).

Sweeps in longitudinal field geometry Since we did not observe any apparent signal related to the polar Kerr effect, we moved to the geometry suitable for an observation of the Voigt effect. The Voigt effect is an even function of effective magnetization (an analogue of transverse AMR) and therefore is also present in conventional, fully compensated antiferromagnets [66].

The measurement of the field sweeps in longitudinal geometry was analogous to the polar configuration: the magnetic field was swept between ±900 mT, and we experimented with various temperatures and polarization orientations. Here, the polarization dependence was particularly important since the Voigt effect is

strongly polarization-dependent [11]. The field orientation was parallel to the sample surface. This enabled us to do the measurement with a lower noise level since the incident beam did not pass the aperture in the pole piece (see Fig. 3.7).

The measurement was done at several temperatures between 30 K and 296 K. To suppress any parasitic signal originating in the cryostat windows, we subtracted a curve measured at room temperature from all the presented measurements. Note also that each curve is an average of multiple sweeps, usually twenty.

Fig. 3.12a shows a field dependence of β_{MO} measured in the `MnSi82` sample at four different temperatures. The data are shown for two different polarization orientations of $\theta = 0°$ and $\theta = 45°$. The signal significantly depends on the applied magnetic field at 30 K and 120 K, which becomes negligible around 200 K. The detected signals at lower temperatures are an even (quadratic) function of the external magnetic field. This, in principle, agrees with the dependence we would expect, since the longitudinal field configuration should be sensitive to the magnetooptical Voigt effect in reflection. The VER is quadratic in the magnetic field, which is analogical to AMR (see Fig. 2.8). However, the observed magnetooptical signal seems to be polarization independent while the magnetooptical Voigt effect depends on the angle between the polarization and magnetization [11, 64, 66].

In order to unveil the origin of the observed signals, we further focused on its dependence on the wavelength, which was investigated in the sample `MnSi80`. The signals were again detected at different temperatures to distinguish between the individual magnetic states of the material, as shown in Fig. 3.12b. We measured the field sweeps using two wavelengths of the incident light: 405 nm in the UV region and 785 nm in the near IR. Note that in this measurement, we managed to decrease the noise level to the peak-to-peak amplitude of 10 μrad. We again observed a quadratic-like dependence of β_{MO} on the external magnetic field that decreases with increasing temperature. The same feature is present for both the wavelengths (see Fig. 3.12b). The only exception is the measurement at 210 K where a substantial signal appears for the wavelength of 785 nm, which is even more pronounced than those at lower temperatures of 180 K and 120 K. The origin of this effect remains yet to be resolved, but it may have happened that the removal of the room-temperature artefact failed in this specific measurement. Otherwise, the magnetooptical signal measured using 785 nm has a similar or higher magnitude compared to those for the wavelength of 405 nm.

To further confirm the magnetic origin of our signals, we also did a control measurement on a plain Si(100) substrate at the same temperatures as in the case of Mn_5Si_3. These are shown for comparison both in Fig. 3.12a and in Fig. 3.12b for the wavelength of 785 nm and $\theta = 0°$. Within our noise level, there is no magnetic-field dependent signal. This leads us to the conclusion that the magnetooptical signal we observe in `MnSi80` and `MnSi82` is related to the Mn_5Si_3 layers, and it cannot be explained in terms of a measurement-system artefact. The temperature dependence of the signal supports this claim, as it vanishes around 200 K, close to the Néel phase transition (around 210 K).

In conclusion, we observe signals quadratic in a magnetic field that are correlated with temperature similarly to the magnetic ordering in Mn_5Si_3. However, to attribute them unambiguously to the Voigt effect, further experiments, such as a detailed spectral dependence or more extensive studies on various samples are needed.

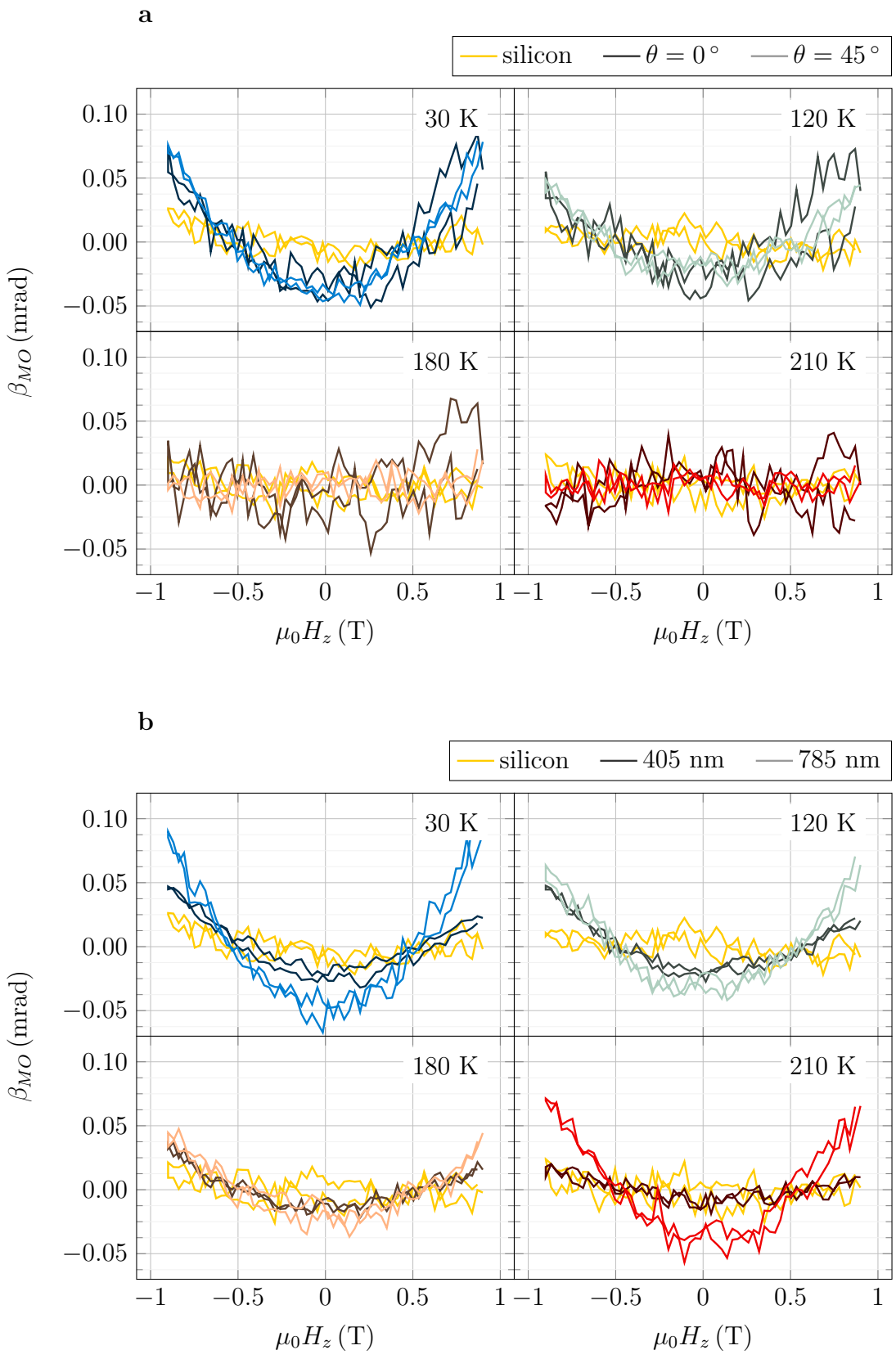

Figure 3.12: Dependence of the rotation of polarization plane β_{MO} on the applied in-plane magnetic field during a longitudinal field sweep for **a** the sample `MnSi82` and **b** the sample `MnSi80`. Both panels include a control measurement on a Si(100) substrate, with the laser wavelength of 785 nm and $\theta = 0°$. **a** The data are shown for two polarization orientations $\theta = 0°$ and $\theta = 45°$ and were measured using 785-nm laser light. **b** Sweeps were measured using 405 nm and 785 nm with $\theta = 0°$.

Conclusion

This work aimed to study thin epilayers of antiferromagnetic Mn_5Si_3 by means of magnetooptical and magnetotransport measurements. Mn_5Si_3 is an example of the recently proposed class of collinear antiferromagnets that show nonrelativistic spin-splitting — altermagnets. Since the idea of altermagnetism was first formulated in 2020 [48] and formalized only very recently [7], there is a limited number of experimental studies available on these materials.

The measurement of magnetotransport properties of Mn_5Si_3 was performed on a patterned sample of Mn_5Si_3 thin epilayer. Firstly, we complemented our previous measurements of electronic transport [24, 60] with a more detailed analysis of the measured transverse resistance. Namely, we extracted the topological contribution from the field dependence of the transverse signal. We observed that this component is significant in the low-temperature noncollinear phase, and vanishes in the collinear antiferromagnetic phase. In addition, we observed a component of the transverse signal that is even with respect to the applied magnetic field and analyzed it using our novel approach for data processing. This component also scales with temperature and is strongly suppressed in the collinear phase. Although the origin of the latter contribution is not entirely explained, both the described signals serve as useful indicators of the phase transition between the two antiferromagnetic phases of Mn_5Si_3.

The magnetotransport was complemented by the thermoelectric measurements which, however, turned out to be more challenging to perform. The on-chip platinum heater did not provide enough heat gradient to detect any Nernst signal. We were thus forced to use a configuration with external heaters creating a global heat gradient over the entire sample. In this configuration, we measured a nontrivial field-dependent transverse signal that shows a clear saturation at the magnetic fields of approximately 3 T. We attribute this signal to the spontaneous Nernst response of Mn_5Si_3. Surprisingly, the signal does not show any hysteresis as compared to the spontaneous Hall signals, where a clear hysteresis loop developes below the Néel temperature. This lack of loop broadening is still under debate, and we intend to investigate it in more detail. Particularly, we plan to perform an experiment with the simultaneous detection of the Hall and Nernst signals within one measurement.

The presence of both the spontaneous Nernst and Hall effects triggered our search for the complementary magnetooptical signals related to the altermagnetic order. During the magnetooptical study, we probed the magnetooptical response of two epitaxial Mn_5Si_3 samples, very similar to those utilized in transport experiments. We detected large spontaneous Hall conductivity in Mn_5Si_3 and we

thus expected a substantial signal from the polar Kerr effect since both the Hall and the Kerr response depend on the same components of the conductivity tensor (though in a different frequency limits). However, we did not observe any reliable Kerr signal even though we probed the samples by a light of different wavelengths and polarization orientations. This may have been caused by the high noise level due to the constraints of our experimental setup.

In contrast, in the Voigt geometry, where we detected the magnetooptical signal as a function of the magnetic field applied in the sample plane, we observed a signal that could be possibly attributed to the magnetooptical Voigt effect. We suppose that this signal arises from the Mn_5Si_3 layer. However, its origin is still under discussion since the polarization dependence (or a lack of it) does not correspond to that expected for the Voigt effect.

The magnetooptical experiments were concluded by measuring the temperature dependence of the polarization signals in two configurations: In the first one, the sample was directly glued on a copper sample holder, which induced substantial mechanical strain. In the second configuration, the strain was relaxed through multiple silicon layers. The signal measured in the strain-free configuration was of a comparable magnitude to the control measurement on a silicon substrate. However, the first, "strained" configuration resulted in a significant rotation of the polarization plane of approximately 10 mrad, with the most substantial increase of the signal below 100 K. This leads us to the conclusion that mechanical strain can induce a large optical response in Mn_5Si_3, though it is unclear whether it is connected with its magnetic structure.

To the best of our knowledge, there is no magnetooptical study on an altermagnetic material so far, and thus we present the first report of such experiments. The first pioneering measurements of the spontaneous Hall effect has been recently reported in altermagnetic RuO_2 [85] and Mn_5Si_3 [24]. However, any record of a thermoelectric study of an altermagnetic material is missing. In this thesis, we presented results of the first experiments of this type.

To conclude, this thesis covers the primary characterization of the altermagnetic compound Mn_5Si_3 in terms of its transport and magnetooptical properties. Some of these experiments were the first attempts in this novel class of magnetic materials. A natural consequence is that we raised more questions than we were able to answer and that much more experiments have to be done to provide definite conclusions.

Bibliography

[1] Shalf, J. The future of computing beyond Moores Law. *Philosophical Transactions of the Royal Society A* **378,** 20190061 (2020).

[2] Marković, D., Mizrahi, A., Querlioz, D. & Grollier, J. Physics for neuromorphic computing. *Nature Reviews Physics* **2,** 499–510 (2020).

[3] Wolf, S. A. *et al.* Spintronics: A spin-based electronics vision for the future. *Science* **294,** 1488–1495 (2001).

[4] Hirohata, A. *et al.* Review on spintronics: Principles and device applications. *Journal of Magnetism and Magnetic Materials* **509,** 166711 (2020).

[5] Baltz, V. *et al.* Antiferromagnetic spintronics. *Reviews of Modern Physics* **90,** 015005 (2018).

[6] Olejník, K. *et al.* Antiferromagnetic CuMnAs multi-level memory cell with microelectronic compatibility. *Nature Communications* **8,** 1–7 (2017).

[7] Šmejkal, L., Sinova, J. & Jungwirth, T. Altermagnetism: spin-momentum locked phase protected by non-relativistic symmetries. *arXiv e-prints,* 2105.05820 (2021).

[8] Coey, J. M. *Magnetism and magnetic materials* 1st edition (Cambridge University Press, 2010).

[9] Dirac, P. A. M. The quantum theory of the electron. *Proceedings of the Royal Society of London A* **117,** 610–624 (1928).

[10] Blundell, S. *Magnetism in Condensed Matter* 1st edition (Oxford University Press, 2001).

[11] Janda, T. *Investigation of spin structure and dynamics in magnetically ordered thin films* PhD thesis (Charles University, 2020).

[12] Saidl, V. *et al.* Investigation of magneto-structural phase transition in FeRh by reflectivity and transmittance measurements in visible and near-infrared spectral region. *New Journal of Physics* **18,** 083017 (2016).

[13] Collins, M. F. & Petrenko, O. A. Triangular antiferromagnets. *Canadian Journal of Physics* **75,** 605–655 (1997).

[14] Gomonaj, E. V. Magnetostriction and piezomagnetism of noncollinear antiferromagnet Mn_3NiN. *Phase Transitions* **18,** 93–101 (1988).

[15] Girtu, M., Wynn, C., Fujita, W., Awaga, K. & Epstein, A. Coexistence of glassiness and canted antiferromagnetism in triangular quantum Heisenberg antiferromagnets with weak Dzyaloshinskii-Moriya interaction. *Physical Review B* **57,** R11058 (1998).

[16] Chen, H., Niu, Q. & Macdonald, A. H. Anomalous Hall effect arising from noncollinear antiferromagnetism. *Physical Review Letters* **112,** 017205 (2014).

[17] Nagaosa, N., Sinova, J., Onoda, S., MacDonald, A. H. & Ong, N. P. Anomalous Hall effect. *Reviews of Modern Physics* **82,** 1539 (2010).

[18] Turek, I. Altermagnetism and magnetic groups with pseudoscalar electron spin. *arXiv e-prints,* 2201.11452 (2022).

[19] Armitage, N. P., Mele, E. J. & Vishwanath, A. Weyl and Dirac semimetals in three-dimensional solids. *Reviews of Modern Physics* **90,** 015001 (2018).

[20] Ahn, K. H., Hariki, A., Lee, K. W. & Kuneš, J. Antiferromagnetism in RuO_2 as d-wave Pomeranchuk instability. *Physical Review B* **99,** 184432 (2019).

[21] Yuan, L. D., Wang, Z., Luo, J. W., Rashba, E. I. & Zunger, A. Giant momentum-dependent spin splitting in centrosymmetric low-Z antiferromagnets. *Physical Review B* **102,** 014422 (2020).

[22] González-Hernández, R. *et al.* Efficient electrical spin splitter based on nonrelativistic collinear antiferromagnetism. *Physical Review Letters* **126,** 127701 (2021).

[23] Litvin, D. B. Spin point groups. *Acta Crystallographica Section A* **33,** 279–287 (1977).

[24] Reichlová, H. *et al.* Macroscopic time reversal symmetry breaking by staggered spin-momentum interaction. *arXiv e-prints,* 2012.15651 (2020).

[25] Biniskos, N. *et al.* Complex magnetic structure and spin waves of the noncollinear antiferromagnet Mn_5Si_3. *Physical Review B* **105,** 104404 (2022).

[26] Songlin *et al.* Magnetic phase transition and magnetocaloric effect in $Mn_{5-x}Fe_xSi_3$. *Journal of Alloys and Compounds* **334,** 249–252 (2002).

[27] Das, S. C., Mandal, K., Dutta, P., Pramanick, S. & Chatterjee, S. Observation of inverted hysteresis loop and thermomagnetic irreversibility in the antiferromagnetic Mn_5Si_3 alloy. *Physical Review B* **100,** 024409 (2019).

[28] Sürgers, C., Fischer, G., Winkel, P. & Löhneysen, H. V. Large topological Hall effect in the non-collinear phase of an antiferromagnet. *Nature Communications* **5,** 1–8 (2014).

[29] Sürgers, C., Kittler, W., Wolf, T. & Löhneysen, H. V. Anomalous Hall effect in the noncollinear antiferromagnet Mn_5Si_3. *AIP Advances* **6,** 055604 (2016).

[30] Sürgers, C. *et al.* Switching of a large anomalous Hall effect between metamagnetic phases of a non-collinear antiferromagnet. *Scientific Reports* **7,** 1–7 (2017).

[31] Luccas, R. F. *et al.* Magnetic phase diagram, magnetotransport and inverse magnetocaloric effect in the noncollinear antiferromagnet Mn_5Si_3. *Journal of Magnetism and Magnetic Materials* **489,** 165451 (2019).

[32] Biniskos, N. *et al.* Spin Fluctuations Drive the Inverse Magnetocaloric Effect in Mn_5Si_3. *Physical Review Letters* **120,** 257205 (2018).

[33] Gottschilch, M. *et al.* Study of the antiferromagnetism of Mn_5Si_3: an inverse magnetocaloric effect material. *Journal of Materials Chemistry* **22,** 15275–15284 (2012).

[34] Brown, P. J. & Forsyth, J. B. Antiferromagnetism in Mn_5Si_3: the magnetic structure of the AF2 phase at 70 K. *Journal of Physics: Condensed Matter* **7,** 7619 (1995).

[35] Santos, F. J. *et al.* Spin waves in the collinear antiferromagnetic phase of Mn_5Si_3. *Physical Review B* **103,** 024407 (2021).

[36] Brown, P. J., Forsyth, J. B., Nunez, V. & Tasset, F. The low-temperature antiferromagnetic structure of Mn_5Si_3 revised in the light of neutron polarimetry. *Journal of Physics: Condensed Matter* **4,** 10025 (1992).

[37] Hall, E. H. On a new action of the magnet on electric currents. *American Journal of Mathematics* **2,** 287–292 (1879).

[38] Frank, H. *Fyzika a technika polovodičů (in Czech)* 1st edition (Státní nakladatelství technické literatury, 1990).

[39] Hall, E. H. On the "Rotational Coefficient" in nickel and cobalt. *The London, Edinburgh, and Dublin Philosophical Magazine and Journal of Science* **12,** 325 (1881).

[40] Pugh, E. M. & Lippert, T. W. Hall e.m.f. and intensity of magnetization. *Physical Review* **42,** 709 (1932).

[41] Smith, A. W. The variation of the Hall effect in metals with change of temperature. *Physical Review (Series I)* **30,** 1 (1910).

[42] Karplus, R. & Luttinger, J. M. Hall effect in ferromagnetics. *Physical Review* **95,** 1154 (1954).

[43] Sakurai, J. J. & Napolitano, J. *Modern Quantum Mechanics* 3rd edition (Cambridge University Press, 2020).

[44] Landau, L. D., Lifshitz, E. M. & King, A. L. Electrodynamics of Continuous Media. *American Journal of Physics* **29,** 647 (1961).

[45] Ikeda, T. *et al.* Anomalous Hall effect in polycrystalline Mn_3Sn thin films. *Applied Physics Letters* **113,** 222405 (2018).

[46] Kiyohara, N., Tomita, T. & Nakatsuji, S. Giant Anomalous Hall Effect in the Chiral Antiferromagnet Mn_3Ge. *Physical Review Applied* **5,** 064009 (2016).

[47] Liu, Z. H. *et al.* Transition from Anomalous Hall Effect to Topological Hall Effect in Hexagonal Non-Collinear Magnet Mn_3Ga. *Scientific Reports* **7,** 1–7 (2017).

[48] Šmejkal, L., González-Hernández, R., Jungwirth, T. & Sinova, J. Crystal time-reversal symmetry breaking and spontaneous Hall effect in collinear antiferromagnets. *Science Advances* **6,** eaaz8809 (2020).

[49] Bruno, P., Dugaev, V. K. & Taillefumier, M. Topological Hall effect and Berry phase in magnetic nanostructures. *Physical Review Letters* **93,** 096806 (2004).

[50] Yanagihara, H. & Salamon, M. B. Skyrmion Strings and the Anomalous Hall Effect in CrO_2. *Physical Review Letters* **89,** 187201 (2002).

[51] Taylor, J. M. *et al.* Anomalous and topological Hall effects in epitaxial thin films of the noncollinear antiferromagnet Mn_3Sn. *Physical Review B* **101,** 094404 (2020).

[52] Gu, H. *et al.* An overview of the magnetoresistance phenomenon in molecular systems. *Chemical Society Reviews* **42,** 5907–5943 (2013).

[53] Fina, I. *et al.* Anisotropic magnetoresistance in an antiferromagnetic semiconductor. *Nature Communications* **5,** 1–7 (2014).

[54] Xiao, D., Yao, Y., Fang, Z. & Niu, Q. Berry-phase effect in anomalous thermoelectric transport. *Physical Review Letters* **97,** 026603 (2006).

[55] Goldsmid, H. J. *Introduction to Thermoelectricity* 1st edition (Springer Berlin Heidelberg, 2016).

[56] Behnia, K. & Aubin, H. Nernst effect in metals and superconductors: A review of concepts and experiments. *Reports on Progress in Physics* **79,** 046502 (2016).

[57] Park, G. H. *et al.* Thickness dependence of the anomalous Nernst effect and the Mott relation of Weyl semimetal Co_2MnGa thin films. *Physical Review B* **101,** 060406 (2020).

[58] Ikhlas, M. *et al.* Large anomalous Nernst effect at room temperature in a chiral antiferromagnet. *Nature Physics* **13,** 1085–1090 (2017).

[59] Reichlová, H. *Nanostructures and Materials for Antiferromagnetic Spintronics* PhD thesis (Institute of Physics ASCR, 2015).

[60] Bad'ura, A. *Thermo-transport effects in antiferromagnets* Bachelor thesis (Charles University, 2020).

[61] Sheng, P., Fujita, T. & Mizuguchi, M. Anomalous Nernst effect in $Co_x(MgO)_{1-x}$ granular thin films. *Applied Physics Letters* **116,** 142403 (2020).

[62] Wang, Y. *et al.* Antisymmetric linear magnetoresistance and the planar Hall effect. *Nature Communications* **11,** 1–8 (2020).

[63] Schlitz, R. *et al.* All Electrical Access to Topological Transport Features in $M_{1.8}PtSn$ Films. *Nano Letters* **19,** 2366–2370 (2019).

[64] Zvezdin, A. K. & Kotov, V. A. *Modern Magnetooptics and Magnetooptical Materials* 1st edition (Taylor and Francis, 1997).

[65] Saidl, V. *et al.* Optical determination of the Néel vector in a CuMnAs thin-film antiferromagnet. *Nature Photonics* **11,** 91–96 (2017).

[66] Tesařová, N. *et al.* Systematic study of magnetic linear dichroism and birefringence in (Ga,Mn)As. *Physical Review B* **89,** 085203 (2014).

[67] Višnovský, S. Magneto-optical permittivity tensor in crystals. *Czechoslovak Journal of Physics B* **36,** 1424–1433 (1986).

[68] Jain, A. *et al.* The Materials Project: A materials genome approach to accelerating materials innovation. *APL Materials* **1,** 011002 (2013).

[69] Kim, M. H. *et al.* Determination of the infrared complex magnetoconductivity tensor in itinerant ferromagnets from Faraday and Kerr measurements. *Physical Review B* **75,** 214416 (2007).

[70] Feng, W., Guo, G. Y., Zhou, J., Yao, Y. & Niu, Q. Large magneto-optical Kerr effect in noncollinear antiferromagnets Mn_3X (X=Rh, Ir, Pt). *Physical Review B* **92,** 144426 (2015).

[71] Higo, T. *et al.* Large magneto-optical Kerr effect and imaging of magnetic octupole domains in an antiferromagnetic metal. *Nature Photonics* **12,** 73–78 (2018).

[72] Kim, M. H. *et al.* Infrared anomalous Hall effect in $SrRuO_3$: Exploring evidence for crossover to intrinsic behavior. *Physical Review B* **81,** 235218 (2010).

[73] Lu, H. S. & Guo, G. Y. Anomalous ferromagnetism and magneto-optical Kerr effect in semiconducting double perovskite Ba_2NiOsO_6 and its (111) $(Ba_2NiOsO_6)/(BaTiO_3)_{10}$ superlattice. *Physical Review B* **100,** 054443 (2019).

[74] Balk, A. L. *et al.* Comparing the anomalous Hall effect and the magneto-optical Kerr effect through antiferromagnetic phase transitions in Mn_3Sn. *Applied Physics Letters* **114,** 032401 (2019).

[75] Acbas, G. *et al.* Electronic structure of ferromagnetic semiconductor $Ga_{1-x}Mn_xAs$ probed by subgap magneto-optical spectroscopy. *Physical Review Letters* **103,** 137201 (2009).

[76] Ferre, J & Gehring, G. A. Linear optical birefringence of magnetic crystals. *Reports on Progress in Physics* **47,** 513 (1984).

[77] Ishikawa, Y., Tajima, K., Bloch, D. & Roth, M. Helical spin structure in manganese silicide MnSi. *Solid State Communications* **19,** 525–528 (1976).

[78] Papatryfonos, K. *et al.* Refractive indices of MBE-grown $Al_xGa_{1-x}As$ ternary alloys in the transparent wavelength region. *AIP Advances* **11,** 025327 (2021).

[79] Schinke, C. *et al.* Uncertainty analysis for the coefficient of band-to-band absorption of crystalline silicon. *AIP Advances* **5,** 067168 (2015).

[80] Michels, W. C. & Curtis, N. L. A pentode lock-in amplifier of high frequency selectivity. *Review of Scientific Instruments* **12,** 444–447 (1941).

[81] Saidl, V. *Ultrarychlá laserová spektroskopie antiferomagnetů (in Czech)* PhD thesis (Charles University, 2018).

[82] White, G. K. Thermal expansion of reference materials: copper, silica and silicon. *Journal of Physics D* **6,** 2070 (1973).

[83] Zhou, X. *et al.* Spin-order dependent anomalous Hall effect and magneto-optical effect in the noncollinear antiferromagnets Mn_3XN with X=Ga, Zn, Ag, or Ni. *Physical Review B* **99,** 104428 (2019).

[84] Johnson, F. *et al.* Room temperature weak collinear ferrimagnet with symmetry driven, large intrinsic magneto-optic and magneto-transport signatures. *arXiv e-prints,* 2111.13498 (2021).

[85] Feng, Z. *et al.* Observation of the Anomalous Hall Effect in a Collinear Antiferromagnet. *arXiv e-prints,* 2002.08712 (2020).

List of Figures

List of Abbreviations

AF	an antiferromagnet, antiferromagnetic,
AFM	an antiferromagnet, antiferromagnetic,
AHE	the anomalous Hall effect,
AMR	anisotropic magnetoresistance,
ANE	the anomalous Nernst effect,
ASA	acrylonitrile styrene acrylate,
cAFM	collinear antiferromagnetic (ordering, phase),
FM	a ferromagnet, ferromagnetic,
MO	magnetooptics, magnetooptical,
MR	magnetoresistance,
nAFM	noncollinear antiferromagnetic (ordering, phase),
OHE	the ordinary Hall effect,
ONE	the ordinary Nernst effect,
PM	a paramagnet,
PMOKE	the polar magnetooptical Kerr effect,
SOI	the spin–orbit interaction,
ATMR	anisotropic thermal magnetoresistance,
THE	the topological Hall effect,
VER	the Voigt effect in reflection.